ôParameterization of Vertical Turbulent Transport in the Inner Core of Tropical Cyclones and Its Impact on Storm Intensification. Part I: Sensitivity to Turbulent Mixing Length*◎*

JEREMY KATZ^a AND PING ZHU^{Da}

^a Department of Earth and Environment, Florida International University, Miami, Florida

(Manuscript received 22 December 2023, in final form 16 July 2024, accepted 7 August 2024)

ABSTRACT: In the inner core of a tropical cyclone, turbulence not only exists in the boundary layer (BL) but can also be generated above the BL by eyewall and rainband clouds. Thus, the treatment of vertical turbulent mixing must go beyond the conventional scope of the BL. The turbulence schemes formulated based on the turbulent kinetic energy (TKE) are attractive as they are applicable to both deep and shallow convection regimes in the tropical cyclone (TC) inner core provided that the TKE production and dissipation can be appropriately determined. However, TKE schemes are not self-closed. They must be closed by an empirically prescribed vertical profile of mixing length. This motivates this study to investigate the sensitivity of the simulated TC intensification to the sloping curvature and asymptotic length scale of mixing length, the two parameters that determine the vertical distribution of a prescribed mixing length. To tackle the problem, both idealized and real-case TC simulations are performed. The results show that the simulated TC intensification is sensitive to the sloping curvature of mixing length but only exhibits marginal sensitivity to the asymptotic length scale. The underlying reasons for such sensitivities are explored analytically based on the Mellor and Yamada level-2 turbulence model and the analyses of azimuthal-mean tangential wind budget. The results highlight the uncertainty and importance of mixing length in the numerical prediction of TCs and suggest that future research should focus on searching for physical constraints on mixing length, particularly in the low- to midtroposphere, using observations and large-eddy simulations.

SIGNIFICANCE STATEMENT: The parametric representation of subgrid-scale turbulent mixing is one of the major sources of uncertainty in numerical predictions of tropical cyclones (TCs). This study investigates how the numerical prediction of TC intensification is affected by the turbulent mixing length, a length scale that is required to close a turbulence scheme formulated based on the turbulent kinetic energy (TKE). The research highlights the uncertainty and importance of mixing length in numerical prediction of TCs and suggests that future research should focus on searching for physical constraints on the mixing length, particularly in the low- to midtroposphere, using observations and large-eddy simulations.

KEYWORDS: Turbulence; Tropical cyclones; Numerical analysis/modeling; Parameterization

1. Introduction

Accurate prediction of tropical cyclone (TC) intensification, in particular, rapid intensification (RI), remains a great challenge in numerical weather prediction (NWP) despite the fact that the state-of-the-art operational models have sufficient resolutions to resolve large-scale fields, sophisticated data assimilation to initialize TC vortices, and a coupled ocean component to account for air–sea interaction. One of the problems stems from the numerical methods of using discretized grids to simulate the continuous atmospheric flow so

Openotes content that is immediately available upon publication as open access.

© Supplemental information related to this paper is available at the Journals Online website: https://doi.org/10.1175/JAS-D-23-0242.s1.

Corresponding author: Ping Zhu, zhup@fiu.com

that the subgrid-scale (SGS) turbulent processes must be represented parametrically.

The importance of turbulent processes to storm development has been long recognized. Theories for TC intensification from the conditional instability of the second kind (CISK, Charney and Eliassen 1964; Ooyama 1964), cooperativeintensification mechanism (Ooyama 1982), and wind-induced surface heat exchange (WISHE, Emanuel 1986) to the advanced three-dimensional rotating convective updraft paradigm (Montgomery and Smith 2014) all recognized the critical role of turbulent transport in TC intensification. Turbulent processes can affect TC evolution in multiple ways. First, the turbulence-induced friction breaks down the gradient-wind balance and results in the radial inflow in the boundary layer (BL). As the air converges toward the storm center, it erupts out of the BL and diverges out along the eyewall, causing the spindown of a TC vortex to conserve its angular momentum. Second, turbulence transports the energy obtained from the ocean surface to foster eyewall convection, which creates a converging spinup mechanism to counteract the diverging spindown process. Third, the radial inflow advects the absolute vorticity inward toward the eyewall, leading to the vortex

DOI: 10.1175/JAS-D-23-0242.1

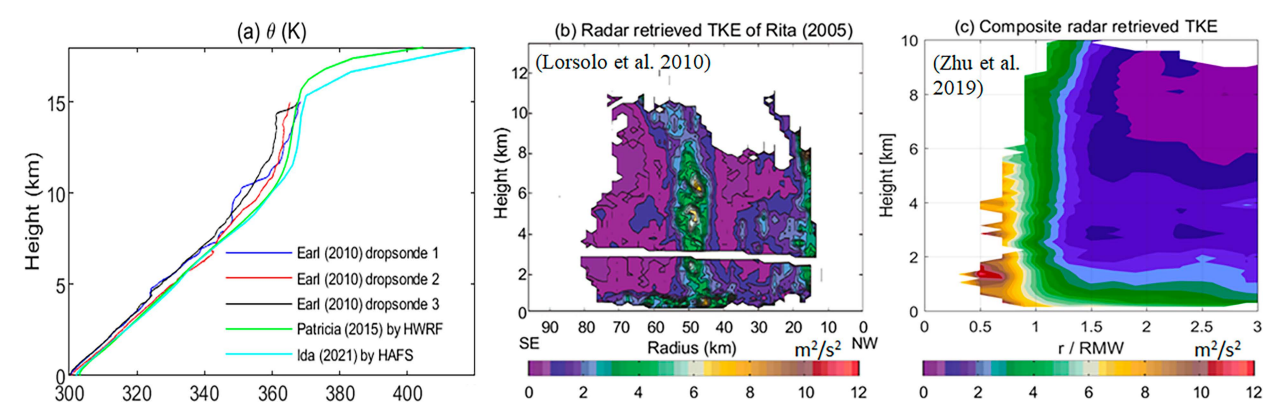


FIG. 1. (a) Vertical profiles of the potential temperature θ in the eyewall from the dropsondes collected in Hurricane Earl (2010) and those from Hurricanes Patricia (2015) and Ida (2021) simulated by HWRF and HAFS, respectively. (b) TKE in Hurricane Rita (2005) at 1913 UTC 22 Sep 2005, derived from the airborne Doppler radar observations (after Lorsolo et al. 2010). (c) Composite TKE from 116 radial legs of P3 flights in the 2003–10 hurricane seasons as a function of height and the radius normalized by RMW (after Zhu et al. 2019).

acceleration if the inward transport of absolute vorticity exceeds that removed by the frictional torque, known as the BL spinup mechanism (Smith et al. 2009). Since these individual mechanisms are intertwined together, it remains unclear how they interact with each other leading to the net acceleration or deceleration of a TC vortex. The problem is further complicated in numerical simulations as these processes depend largely on how turbulence is parameterized. This constitutes a major uncertainty in the numerical predication of TC intensification.

The SGS turbulence is commonly regarded as a flow feature pertaining to the BL. In the typical continental convective BL (CBL), marine BL (MBL) topped by stratocumulus or shallow cumulus, and nocturnal stable BL (SBL), the turbulent BL is cleanly separated from the free atmosphere above by a capping inversion. Because of this, historically, the vertical turbulent mixing below and above the BL is often treated separately, and this parameterization strategy has been adopted in many vertical turbulent mixing schemes, such as the Yonsei University (YSU) scheme (Hong et al. 2006), the NCEP Global Forecast System (GFS) scheme (Hong and Pan 1996), eddy-diffusivity mass-flux (EDMF) hybrid PBL scheme (Han et al. 2016), the Asymmetric Convective Model, version 2 (ACM2), scheme (Pleim 2007), and the Grenier-Bretherton scheme (Grenier and Bretherton 2001). These schemes, which were developed and validated using the typical CBL, MBL, and SBL, have also been widely used in TC simulations including operational forecasts of TCs.

However, studies show that turbulent processes in the inner core of a TC, particularly in the eyewall and rainbands, have unique characteristics different from that of CBL, MBL, and SBL (e.g., Moss and Rosenthal 1975; Shapiro 1983; Smith et al. 2008; Smith and Montgomery 2010; Marks et al. 2008; Lorsolo et al. 2010; Zhu et al. 2019, 2021). Figure 1a shows the vertical profiles of the potential temperature θ in the eyewall from the dropsondes collected in Hurricane Earl (2010) along with those in the eyewalls of Hurricane Patricia (2015) and Hurricane Ida (2021) simulated by the Hurricane Weather Research

and Forecasting Model (HWRF) and the Hurricane Analysis and Forecast System (HAFS) model, respectively. Despite different hurricanes developed under different environmental conditions, the θ profiles in the eyewall of these storms are fairly consistent in the entire troposphere in which no inversion exists to separate the turbulent BL from the free atmosphere above. This unique vertical thermodynamic structure results from the intense turbulent mixing generated by eyewall convective clouds and is starkly different from that of CBL, MBL, and SBL. Figures 1b and 1c show the turbulent kinetic energy (TKE) in Hurricane Rita (2005) retrieved from the airborne Doppler radar observations (Lorsolo et al. 2010) and the composite TKE derived from the radar data collected by 116 radial legs of P3 flights in the 2003-10 hurricane seasons (Zhu et al. 2019). Large TKEs are seen in the eyewall throughout the entire column of the troposphere. Again, no physical interface exists to separate the turbulence generated by the BL processes and cloud process aloft, suggesting that the separate treatment of the turbulence below and above a diagnosed BL currently adopted by many turbulence schemes does not faithfully reflect the observed vertical thermodynamic structure and TKE in the TC eyewall.

One of the methods that may provide vertically integrated parameterization of turbulence is the TKE-based turbulent mixing schemes since they are applicable to both deep and shallow convection regimes regardless of the BL height as long as the shear production, buoyancy production, transport, and dissipation of TKE can be appropriately determined. However, a TKE scheme must be closed by an empirically prescribed turbulent mixing length, which describes the mixing ability of turbulent eddies. To date, most formulae of mixing length used in numerical models were empirically formulated and validated in non-TC conditions. To our knowledge, no comprehensive analysis has been done to examine the sensitivity of the parameterized turbulent processes in the TC inner core and the resultant TC intensification to the prescribed mixing length. Since turbulent processes in the eyewall have unique characteristics different from that of non-TC conditions (Fig. 1), investigation of this issue is of importance to the understanding of the role of turbulence in TC intensification. Moreover, considering that in situ observations of turbulence in TCs are difficult to obtain, such sensitivity tests on turbulence schemes can be further combined with large-eddy simulations (LESs) to address how to realistically represent turbulent processes in TC simulations as illustrated recently by Chen and Bryan (2021), Chen et al. (2021), and Li et al. (2022).

The main objective of this study, therefore, is to investigate how the parameterized turbulent processes in the TC inner core affect the TC intensification. In part I of this study, we examine the sensitivity of TC intensification to the turbulent processes in the TC inner core parameterized by a TKE scheme with differently prescribed turbulent mixing lengths and explore the mechanisms underlying the shown sensitivities. Based on the simulation results, in Part II of this study (Katz and Zhu 2024), we aim to quantify the individual contributions of different dynamic and thermodynamic processes associated with the turbulent mixing to TC intensification in an unbalanced framework using a novel diagnostic tool developed in this study. Utilizing the diagnosed results, we address key issues regarding TC intensification in numerical simulations.

2. A diagnostic "moist" TKE scheme

Historically, all TKE schemes were derived from the hierarchical turbulence closure models proposed by Mellor and Yamada (1974, 1982, MY1974 and MY1982 hereafter). One of them may be developed from level-2 simplification of Mellor–Yamada (MY) models. The advantage of this simplification is that an analytical relationship between turbulent fluxes and vertical gradient of mean variables can be derived (MY1982; Galperin et al. 1988),

$$\begin{cases} \overline{w'u'} = -S_m le \frac{\partial \overline{u}}{\partial z} \\ \overline{w'v'} = -S_m le \frac{\partial \overline{v}}{\partial z}, \\ \overline{w'\theta'} = -S_h le \frac{\partial \overline{\theta}}{\partial z} \end{cases}$$
(1)

where u, v, and w are the wind components in the x, y, and z directions, respectively; overbar and prime indicate the gridbox mean and the perturbation away from the mean; $e^2 = (1/2)(\overline{u'^2} + \overline{v'^2} + \overline{w'^2})$ is the TKE; l is the mixing length; and S_m and S_h are the derived analytical stability functions expressed as

$$\begin{cases} S_{m} = \frac{d_{1} + d_{2}G_{h}}{(1 + d_{3}G_{h})(1 + d_{4}G_{h})} \\ S_{h} = \frac{d_{5}}{1 + d_{3}G_{h}} \\ G_{H} = -\left(\frac{l}{e}\right)^{2}N^{2} \end{cases}, \begin{cases} d_{1} = a_{1}\left(1 - 3c_{1} - 6\frac{a_{1}}{b_{1}}\right) \\ d_{2} = -3a_{1}a_{2}\left[(b_{2} - 3a_{2})\left(1 - 6\frac{a_{1}}{b_{1}}\right) - 3c_{1}(b_{2} + 6a_{1})\right] \\ d_{3} = -3a_{2}(b_{2} + 6a_{1}) \\ d_{4} = -9a_{1}a_{2} \\ d_{5} = a_{2}\left(1 - 6\frac{a_{1}}{b_{1}}\right) \end{cases}, \tag{2}$$

where $N^2 = (g/\overline{\theta})(\partial \overline{\theta}/\partial z)$ is the Brunt-Väisälä frequency and G_H is a dimensionless stability parameter. The variables a_1, a_2, b_1, b_2 , and c_1 are the empirical scaling coefficients and taken as $(a_1, a_2, b_1, b_2, c_1) = (0.92, 0.74, 16.6, 10.1, 0.08)$ in MY1982.

Equation (1) implies that turbulent eddy diffusivity for momentum K_m and heat K_h can be expressed as the function of TKE,

$$\begin{cases}
K_m = leS_m \\
K_h = leS_h
\end{cases}$$
(3)

TKE can be determined from the TKE budget equation,

$$\frac{\partial e^2}{\partial t} = -\overline{u'w'}\frac{\partial \overline{u}}{\partial z} - \overline{v'w'}\frac{\partial \overline{v}}{\partial z} + \frac{g}{\overline{\theta}}\overline{w'\theta'} - \frac{\partial \overline{w'(e^2 + p'/\overline{\rho})}}{\partial z} - \varepsilon,$$

where p is the pressure and ρ is the air density. The terms on the right-hand side (rhs) of Eq. (4) are the TKE shear

production, buoyancy production, transport and pressure correlation, and dissipation, respectively. In practice, TKE may be determined either prognostically by solving Eq. (4) directly or diagnostically by assuming quasi-stationary of TKE over a model time step, i.e., $\partial e^2/\partial t=0$. In this study, we choose the latter since it allows us to derive an analytical solution of TKE under MY level-2 simplification. Assuming that there is a balance among TKE shear production, buoyancy production, and dissipation over a model time step. Neglecting TKE transport and pressure correlation, and parameterizing TKE dissipation in terms of TKE, $\varepsilon=e^3/b_1 l$ (MY1982; Galperin et al. 1988), Eq. (4) reduces to

$$0 = -\overline{u'w'}\frac{\partial \overline{u}}{\partial z} - \overline{v'w'}\frac{\partial \overline{v}}{\partial z} + \frac{g}{\overline{\theta}}\overline{w'\theta'} - \frac{e^3}{b_1 l}.$$
 (5)

Combining Eq. (5) with Eq. (1), it yields

$$e^2 = b_1 l^2 (S_m S^2 - S_h N^2) = b_1 l^2 S^2 (S_m - S_h R_i),$$
 (6)

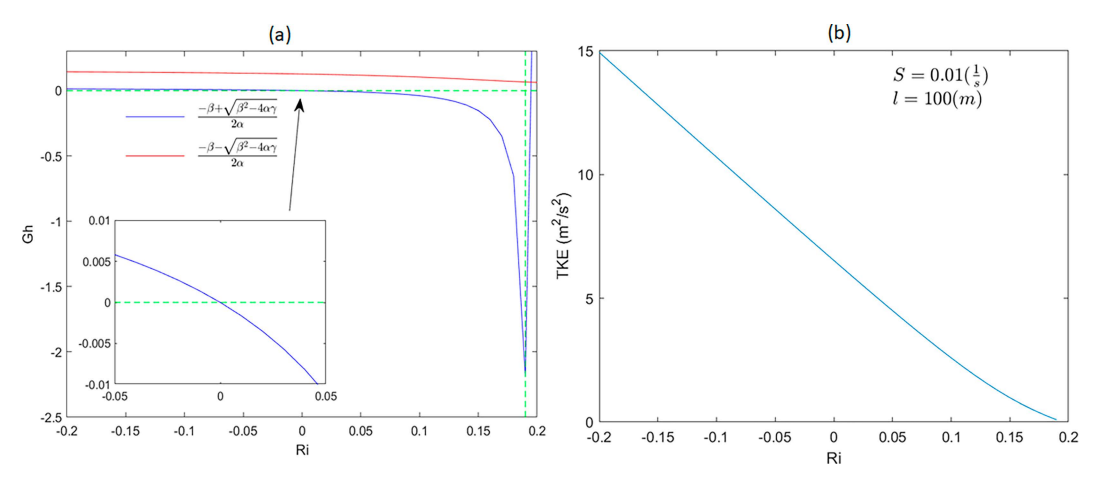


FIG. 2. (a) Change of G_h as a function of R_i predicted by the TKE model. (b) TKE as a function of the R_i for $S = 0.01 \text{ s}^{-1}$ and l = 100 m.

where $S = \sqrt{|\partial \overline{u}/\partial z|^2 + |\partial \overline{v}/\partial z|^2}$ is the magnitude of the vertical wind shear and $R_i = N^2/s^2$ is the gradient Richardson number. Thus, TKE can be diagnosed from Eq. (6)

provided that shear and stability are known. From Eqs. (6) and (2), one can derive a quadratic equation of G_h .

$$\alpha G_h^2 + \beta G_h + \gamma = 0, \dots \begin{cases} \alpha = b_1 d_2 + (d_3 d_4 - b_1 d_4 d_5) R_i = -51.22 + 262.71 R_i \\ \beta = b_1 d_1 + (d_3 + d_4 - b_1 d_5) R_i = 6.53 - 49.00 R_i \\ \gamma = R_i \end{cases}$$
 (7)

The dimensionless stability parameter G_h can be solved from Eq. (7) with a known R_i . For $(a_1, a_2, b_1, b_2, c_1) = (0.92, 0.74,$ 16.6, 10.1, 0.08) in MY1982, it is easy to show that $\beta^2 - 4\alpha \gamma =$ $1350.4R_i^2 - 434.9R_i + 42.6$ is always greater than 0 for all R_i with the minimum $\beta^2 - 4\alpha\gamma = 42.6$ at $R_i = 0$. Thus, Eq. (7) has two real roots $G_h = (-\beta \pm \sqrt{\beta^2 - 4\alpha\gamma})/2\alpha$. It can be shown that the root $G_h = (-\beta - \sqrt{\beta^2 - 4\alpha\gamma})/2\alpha$ is always positive for all R_i (red curve in Fig. 2a); thus, it is unphysical. The other root $G_h = (-\beta + \sqrt{\beta^2 - 4\alpha\gamma})/2\alpha$ can be greater than, equal to, and smaller than 0 for $R_i < 0$, $R_i = 0$, and $R_i > 0$, respectively (blue curve in Fig. 2a); thus, it is a physical solution. Also shown in Fig. 2a, in the stable regime, G_h decreases with the increase of R_i till $R_i = 0.19$. After that, G_h increases, which is unphysical. Therefore, $R_i = 0.19$ may be considered as the critical Richardson number, beyond that there is no turbulence. Once G_h is solved, TKE and eddy exchange coefficients K_m and K_h can be calculated from Eqs. (6) and (3), respectively, provided that the mixing length is known. Note that this TKE scheme does not yield an independent formula for the eddy diffusivity of moisture K_q . Like other turbulent mixing schemes, we treat K_q the same as K_h . Figure 2b shows the variation of TKE as a function of R_i for a given wind shear $S = 0.01 \text{ s}^{-1}$ and mixing length

The system described by Eqs. (1)–(7) provides a concise parameterization of vertical turbulent mixing in terms of the diagnosed TKE. It does not require information of

the BL height as long as the Richardson number at each model level can be accurately determined. However, since the scheme only considers dry thermodynamics in which the Brunt-Väisälä frequency takes the form of $N^2 = (g/\bar{\theta})(\partial\bar{\theta}/\partial z)$, it is not applicable for treating the turbulent processes associated with clouds in TCs. The scheme can be remediated by using a generalized Brunt-Väisälä frequency N^2 that includes the saturated moist thermodynamics. Assuming that an air parcel is in an equilibrium state at z=0, then, for a small vertical displacement δz , it is ready to show that the acceleration of the parcel may be rewritten as

$$a = -N^2 \delta z, \quad N^2 = \frac{g}{\overline{T_v}} \left(\frac{\partial \overline{T_v}}{\partial z} - \frac{\partial T_v^p}{\partial z} \right),$$
 (8)

where T_v is the virtual temperature, g is the gravity, and superscript "p" and overbar denote the air parcel and environment, respectively. Equation (8) may be considered as a generalized Brunt–Väisälä frequency applicable to both unsaturated and saturated atmospheres. For the dry atmosphere, $T_v = T$ and $-(\partial T_v^p/\partial z) = g/C_{pd}$ is simply the dry adiabatic lapse rate, where C_{pd} is the specific heat of dry air at constant pressure; then, Eq. (8) reduces to $N^2 = (g/\overline{\theta})(\partial \overline{\theta}/\partial z)$. Likewise, for the unsaturated atmosphere, it can be shown that Eq. (8) becomes $N^2 = (g/\overline{\theta}_v)(\partial \overline{\theta}_v/\partial z)$, where $\theta_v = T_v(1 + 0.608q_v)$ and q_v are the virtual potential temperature and water vapor mixing ratio, respectively.

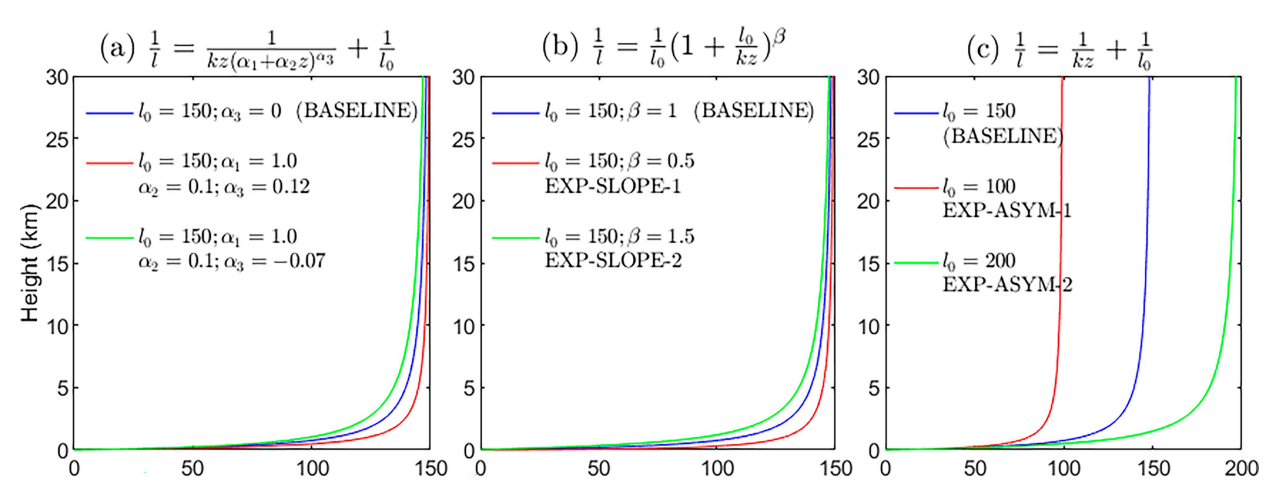


FIG. 3. Mixing length as a function of height calculated using Eqs. (12)–(14) with different parameters and asymptotic length scales l_0 .

In light of $N^2 = (g/\overline{\theta})(\partial \overline{\theta}/\partial z)$ and $N^2 = (g/\overline{\theta}_v)(\partial \overline{\theta}_v/\partial z)$ under dry and unsaturated conditions, for the saturated atmosphere with clouds, one may define a new thermodynamic variable B such that B satisfies

$$N^{2} = \frac{g}{T} \left(\frac{\partial \overline{T_{v}}}{\partial z} - \frac{\partial T_{v}^{p}}{\partial z} \right) = \frac{g}{\overline{B}} \frac{\partial \overline{B}}{\partial z}. \tag{9}$$

Thus, B may be considered as a generic form of θ_{ν} since it can be applied to the saturated atmosphere with clouds to correctly include the buoyancy induced by hydrometeors. With Eq. (9), the dry TKE scheme described by Eqs. (1)–(7) can be remediated by replacing θ with B so that the system can be extended to the saturated atmosphere. The key here is how to accurately calculate $N^2 = (g/\overline{B})(\partial \overline{B}/\partial z)$ for the saturated atmosphere to include the buoyancy induced by clouds. Zhu et al. (2021) showed that for the saturated atmosphere that contains multiple-phase hydrometeors (liquid and solid), the Brunt-Väisälä frequency N^2 may be written as

$$N^{2} \approx g \left[\left(1 + \frac{l_{m} \overline{q_{s}}}{R_{d} \overline{T}} \right) 1 \overline{T} \left(\frac{\partial \overline{T}}{\partial z} + \Gamma_{m} \right) - \frac{1}{1 + \overline{q_{t}}} \frac{\partial \overline{q_{t}}}{\partial z} \right], \tag{10}$$

where q_s and q_t are the mixing ratios of the saturated water vapor and total water (vapor plus hydrometeors), respectively; l_m is the combined specific latent heat of vaporization and sublimation for mixed-phase clouds; R_d is the gas constant for dry air; and Γ_m is the moist adiabatic lapse rate of temperature, which can be expressed as

$$\begin{split} \Gamma_{m} &= -\frac{\partial T^{p}}{\partial z} \\ &= \frac{g}{C_{pd}} \times \frac{(1 + \overline{q_{t}}) \left(1 + \frac{l_{s} \overline{q_{s}}}{R_{d} \overline{T}}\right) + \frac{l_{f} \partial \overline{q_{w}}}{g \partial z}}{1 + \frac{C_{pv} \overline{q_{s}} + C_{w} \overline{q_{w}} + C_{i} \overline{q}_{i}}{C_{pd}} + \frac{(\epsilon + \overline{q_{s}}) l_{s} l_{m} \overline{q_{s}}}{C_{pd} R_{d} \overline{T}^{2}}, \end{split}$$

where C_{pv} , C_w , and C_i are the specific heat of water vapor and liquid and solid hydrometeor, respectively; q_w and q_i are the mixing ratios of liquid and solid hydrometeor, respectively; l_f is the specific latent heat of fusion; and $\epsilon = R_d/R_v$ is the ratio of gas constant for dry air R_d to gas constant of water vapor R_v . The moist TKE scheme described here has been installed in the HWRF version v3.9a for the sensitivity tests performed in this study.

3. Turbulent mixing length

As stated previously, the mixing length in a TKE scheme must be prescribed. An appropriate specification of mixing length needs to reflect the geometry and characteristics of the turbulent flow. For the turbulent atmosphere, the specification of mixing length requires a large measure of guesswork (Pope 2000). In the surface layer, turbulent eddies are constrained by the height; thus, the mixing length is generally considered to be linearly proportional to height, $l = \kappa z$, where $\kappa = 0.4$ is the von Kármán constant (Stull 1988). Above the surface layer, turbulent eddies are less affected by the surface but tend to be constrained by both the capping inversion and the static stability. As a result, the mixing length is commonly parameterized as

$$\frac{1}{l} = \frac{1}{\kappa z} + \frac{1}{l_0},\tag{12}$$

where l_0 is an asymptotic length scale. Since it is difficult to quantify l_0 from observations, l_0 is often simply treated as a constant. In HWRF, l_0 is set to 150 and 30 m for unstable and stable conditions, respectively. However, it remains unknown if such a prescribed mixing length is appropriate for TC simulations. Gopalakrishnan et al. (2021) and Hazelton et al. (2022) showed that modifying the asymptotic length scale based on observations can improve eddy diffusivity parameterization and the overall structure of simulated TCs.

In addition to Eq. (12), other formulae of mixing length have also been formulated. For example, Nakanish (2001) proposed the following formula of mixing length:

TABLE 1. Mixing lengths used in numerical experiments.

Set 1: $\frac{1}{l} = \frac{1}{l_0} \left(1 + \frac{l_0}{kz} \right)^{\beta}$	Set 2: $\frac{1}{l} = \frac{1}{\kappa z} + \frac{1}{l_0}$
$l_0 = 150 \text{ m},$	$l_0 = 150 \text{ m}$
$\beta = 1$ (BASELINE)	(BASELINE)
$l_0 = 150 \text{ m},$	$l_0 = 2000 \text{ m}$
$\beta = 0.5$ (EXP-SLOPE-1)	(EXP-ASYM-1)
$l_0 = 150 \text{ m},$	$l_0 = 100 \text{ m}$
$\beta = 1.5$ (EXP-SLOPE-2)	(EXP-ASYM-2)

$$\frac{1}{l} = \frac{1}{\kappa z (\alpha_1 + \alpha_2 z)^{\alpha_3}} + \frac{1}{l_0},\tag{13}$$

where α_1 , α_2 , and α_3 are the empirical coefficients controlling the sloping curvature of mixing length asymptotically approaching toward l_0 . Equation (13) may be considered as a generalized formula of Eq. (12). For $\alpha_3 = 0$, Eq. (13) reduces to Eq. (12). Equation (13) has been adopted in the TKE EDMF scheme (Han and Bretherton 2019).

Alternatively, the mixing length may be formulated as

$$\frac{1}{l} = \frac{1}{l_0} \left(1 + \frac{l_0}{kz} \right)^{\beta},\tag{14}$$

where β is an empirical coefficient that controls the sloping curvature of mixing length asymptotically approaching toward l_0 . For $\beta = 1$, Eq. (14) reduces to Eq. (12). Figure 3 compares the vertical profiles of mixing length calculated using Eqs. (12)–(14) with different parameters and asymptotic length scale l_0 . For the same l_0 , Eqs. (13) and (14) produce similar vertical profiles.

In this study, two sets of numerical experiments were designed to examine how and why the sloping curvature and the asymptotic length scale l_0 affect TC simulations. In the first set of experiments, the mixing length is calculated using Eq. (14) with the fixed $l_0 = 150$ m but with different values of

 β to obtain different sloping curvatures. In the second set of experiments, the mixing length is calculated using Eq. (12) with three different values of l_0 . Table 1 summarizes the two sets of experiments. Five experiments are performed, which include a baseline experiment and four sensitivity experiments to test the sensitivity of TC intensification to different sloping curvatures (EXP-SLOPE-1 and EXP-SLOPE-2) and different asymptotic length scales (EXP-ASYM-1 and EXP-ASYM-2), respectively.

4. Simulation setup and construction of initial vortex

The model used in this study is the HWRF version v3.9a (https://dtcenter.org/HurrWRF/users/docs/index.php). It consists of triple-nested domains on an E grid. The grid-spacing of the three domains is 0.099°, 0.033°, and 0.011°, respectively, which is equivalent to (or may be slightly higher than) the resolution used by the operational HWRF (approximately 13.5/4.5/1.5 km). The horizontal grid-meshes for the three domains are 390 \times 750, 268 \times 538, and 268 \times 538 km² with 75 levels in the vertical. The physics package includes the Ferrier-Aligo microphysical scheme (Aligo et al. 2018), the modified GFDL longwave/shortwave radiation scheme, the simplified Arakawa-Schubert cumulus scheme for the outmost lowresolution domain, and the modified GFDL surface laver scheme. The only change is that the hybrid EDMF PBL scheme (Han et al. 2016) is replaced by the new moist TKE scheme summarized in section 2.

The idealized HWRF experiments performed in this study are similar to that of Zhu et al. (2015). They are on an f plane with a constant Coriolis parameter at 20°N. The sea surface temperature is set to 29°C. All simulations are initialized with an idealized vortex embedded in a thermodynamic background whose temperature and humidity profiles are specified by the non-Saharan air layer (non-SAL) sounding of Dunion and Marron (2008), which is an updated version of the original Jordan (1958) mean Caribbean hurricane-season sounding.

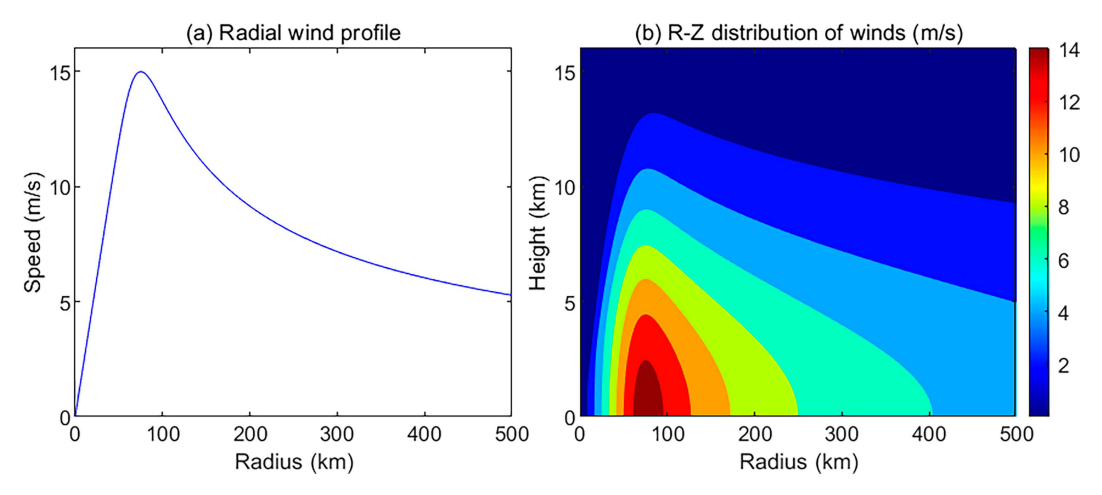


FIG. 4. (a) Radial profile of surface wind. (b) Radius-height structure of the tangential wind of the constructed initial TS vortex.

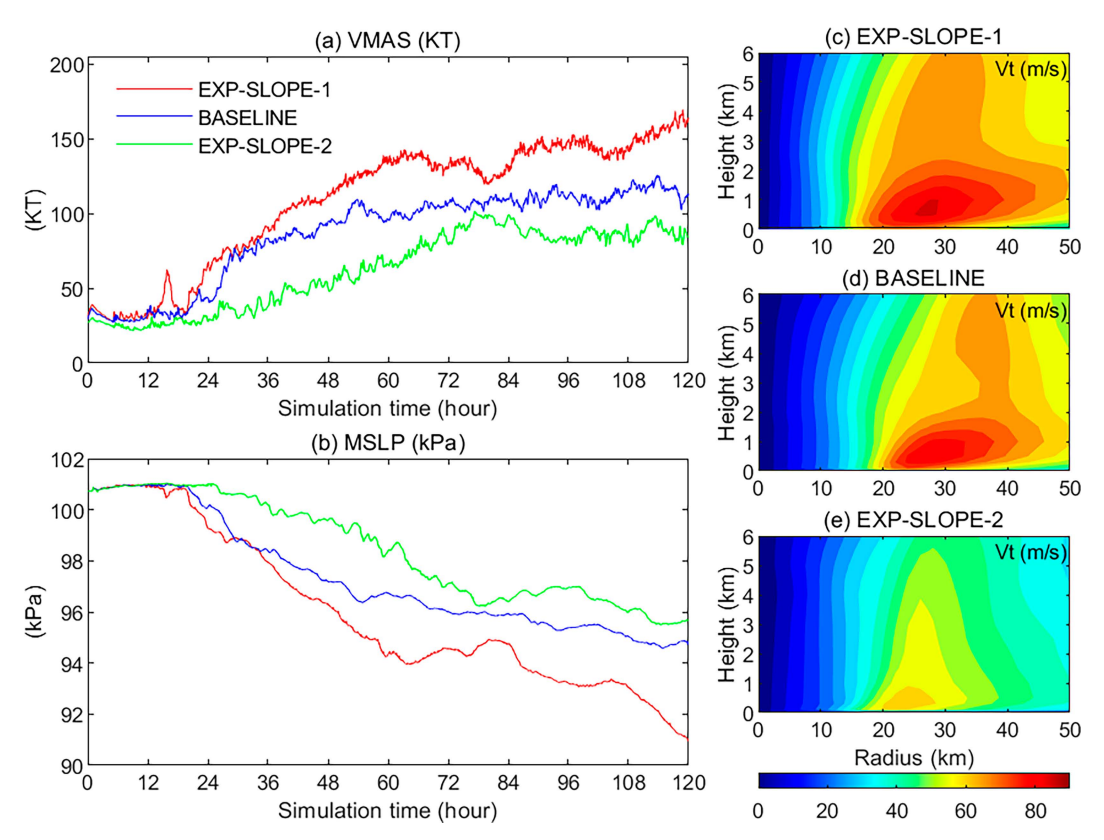


FIG. 5. (a),(b) Time series of VMAX (KT) and MSLP (kPa) from EXP-SLOPE-1 (red), BASELINE (blue), and EXP-SLOPE-2 (green). (c)–(e) Radial–height structure of azimuthal-mean tangential wind at the 120th simulation hour from the three experiments.

The initial vortex has a tropical storm (TS) intensity with an axisymmetric structure. The maximum surface wind speed of 15.0 m s⁻¹ is set at a radius of 75 km. This allows us to examine how it develops into a TC with different intensities in response to differently prescribed mixing lengths. Following Wood and White (2011), the vortex surface tangential wind profile is prescribed by

$$v = v_{\text{max}} \frac{\sigma^k}{\left[1 + k\mu^{-1}(\sigma^{\mu/\lambda} - 1)\right]^{\lambda}}, 0 < k\langle n, \lambda \rangle 0, \tag{15}$$

where $\sigma = r/r_{\rm max}$, k=1, $\mu=1.6$, and $\lambda=0.2$ are the parameters that control the nonlinearity of the inner velocity profile between the vortex center and radius of maximum winds (RMW), the decay of the outer velocity profile, and the radial width of the maximum annular zone of velocity, respectively.

The surface wind profile is then extended into the vertical using an analytic function proposed by Nolan and Montgomery (2002),

$$\nu(z) = \phi \exp\left[-\left(\frac{cz}{z_{\text{top}}}\right)^{\alpha}\right] \left\{1 - \gamma \exp\left[-\left(\frac{r}{\delta + \eta z}\right)^{\epsilon}\right]\right\}, \quad (16)$$

where α , c, γ , δ , η , and ε are the tuning parameters that determine how vortex winds vary with height. The coefficient ϕ

controls the decay of winds with height in a way consistent with that observed in real TCs; z_{top} is the upper limit of the wind field. The $(1 - \gamma \exp\{-[r/(\delta + \eta z)]^{\varepsilon}\})$ modifies the wind field of the eyewall to realistically slope outward with radius and height. Here, the parameters are taken as $z_{\text{top}} = 16 \text{ km}$, $\alpha = 2.0$, c = 1.7, $\varepsilon = 2.7$, $\delta = 1$, $\gamma = 1$, and $\eta = 4.0$. Figure 4 shows the surface wind profile and radius-height structure of tangential winds of the constructed initial TS vortex. Once the initial tangential wind field is constructed, the pressure and temperature fields that hold the vortex are derived to satisfy the hydrostatic and gradient wind balance using the iterative method proposed by Nolan and Montgomery (2002).

5. Results

a. Sensitivities of TC intensification to turbulent mixing length

Five idealized experiments are performed to examine how the constructed axisymmetric TS vortex intensifies in response to differently prescribed mixing lengths under quiescent conditions. All simulations listed in Table 1 are run for 5 days. Here, we first present the sensitivities of TC intensification to different sloping curvatures of mixing length (set 1 experiments) and then examine the sensitivities of TC intensification to different asymptotic length scales (set 2 experiments).

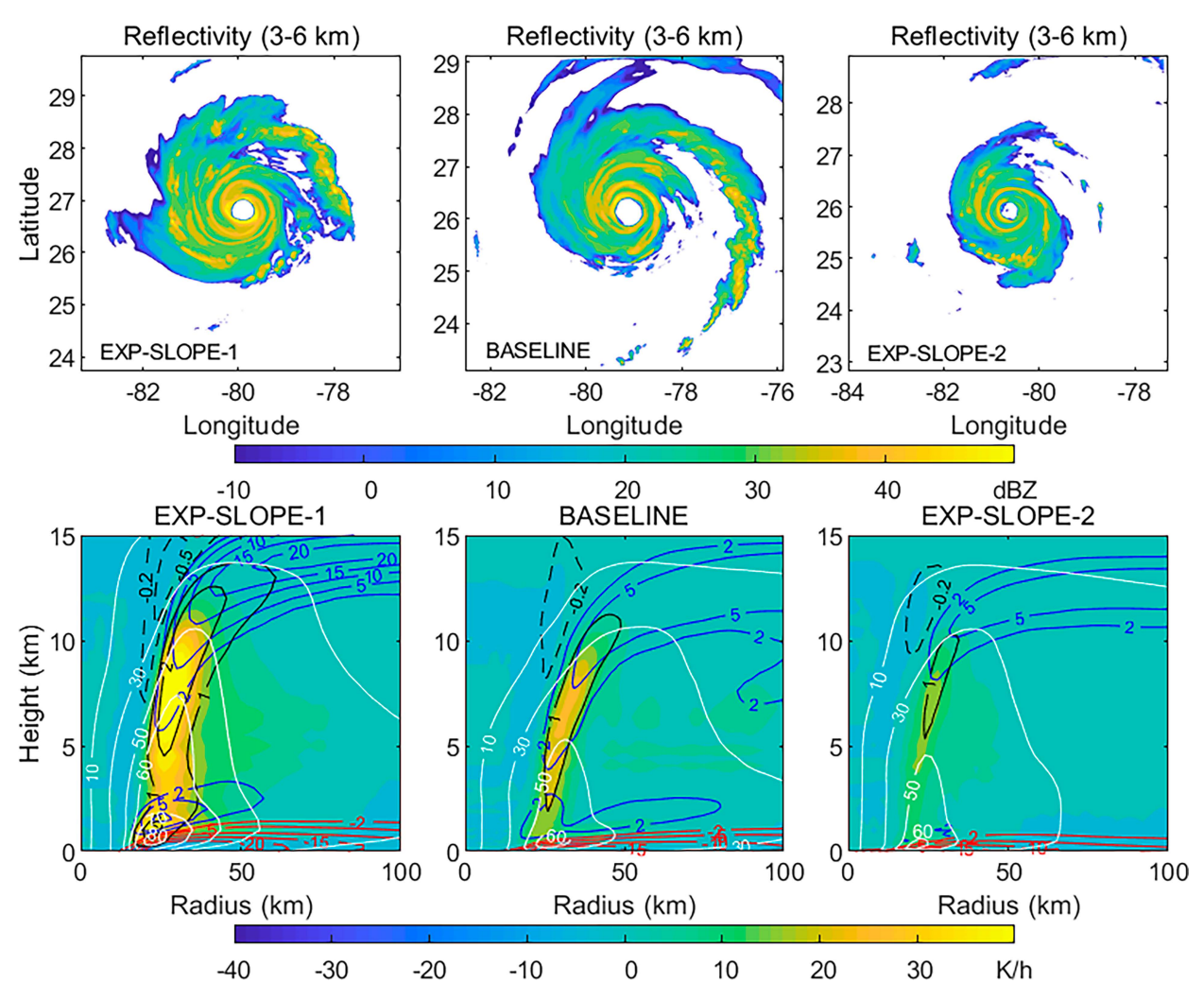


FIG. 6. (top) Radar reflectivity averaged over the altitudes of 3–6 km from EXP-SLOPE-1, BASELINE, and EXP-SLPOE-2. (bottom) Azimuthal-mean radius–height structure of diabatic heating (color shades; K h $^{-1}$); radial inflow (red contours; -2, -5, -10, -5, -20 m s $^{-1}$); radial outflow (blue contours; 2, 5, 10, 15, 20 m s $^{-1}$); updrafts (black contours; 1, 2, 5 m s $^{-1}$); downdrafts (black dashed contours; -0.2, -0.5 m s $^{-1}$); and tangential wind (white contours; 10, 10

Figure 5 shows the time series of surface maximum wind speeds (VMAX) and minimum sea level pressure (MSLP) from the three experiments: EXP-SLOPE-1, BASELINE, and EXP-SLOPE-2 along with their corresponding radial-height structure of azimuthal-mean tangential wind at the 120th simulation hour. The TC vortex undergoes completely different intensification pathways due to the change in the sloping curvature of mixing length. The vortex reaches CAT-5 intensity and merely CAT-2 intensity at the end of a 5-day simulation in EXP-SLOPE-1 and EXP-SLOPE-2, respectively. The vortex intensity in BASELINE is somewhere between EXP-SLOPE-1 and EXP-SLOPE-2. The radial-height structure of the azimuthal-mean tangential wind also confirms that the vortex in EXP-SLOPE-1 is much stronger than that in the other two experiments.

To further illustrate the structural difference of the simulated vortices, The upper panels of Fig. 6 show the horizontal plane

view of the simulated radar reflectivity averaged over 3–6 km in altitudes from the three experiments. In EXP-SLOPE-1, a well-defined eyewall forms a closed convection ring. But in the other two experiments, the eyewall is somewhat broken, and the vortex has a higher degree of asymmetry. The bottom panels of Fig. 6 compare the radial–height structure of the azimuthal-mean diabatic heating, radial flow, tangential wind, and up-/downdrafts averaged over the last 24 h. Of the three experiments, the strongest diabatic heating, tangential wind, radial flow, and eyewall updraft are seen in EXP-SLOPE-1. In section 5b, we will explore how the same initial vortex evolves into different TCs in these three experiments.

One of the motivations of this study is to assess if a moist TKE scheme can realistically represent the large TKE in the eyewall observed by airborne radars (Figs. 1b,c). Figure 7 shows the vertical profiles of TKE in the eyewall averaged over the last 24-h simulations along with the corresponding

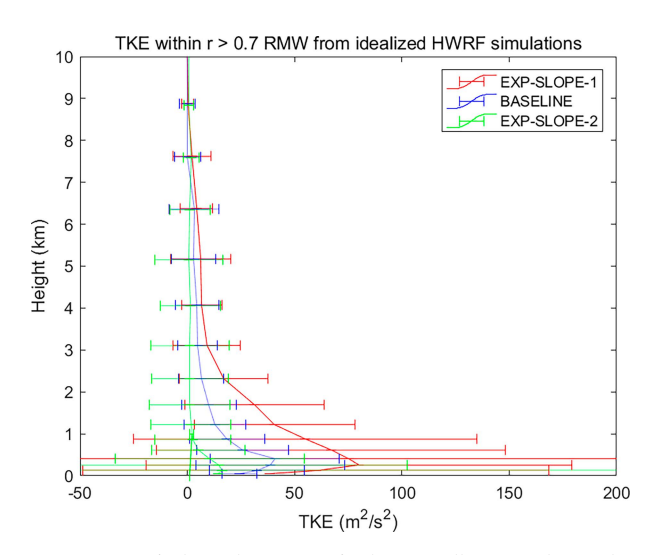


FIG. 7. Vertical profiles of TKE in the eyewall averaged over the last 24-h simulations along with the corresponding standard deviation from the three experiments, BASELINE, EXP_SLOPE-1, and EXP_SLOPE-2.

standard deviations. Large TKE is concentrated in the BL, which mainly results from the shear production of TKE. TKEs are also seen above the BL up to the upper troposphere around 8–9 km, suggesting that the TKE generated by the eyewall clouds is appropriately captured by the TKE scheme. It also shows that the TKE generated in EXP-SLOPE-1 is much larger than that in the other two experiments. The underlying reason will be discussed in section 5c.

Experiments, EXP-ASYM-1 and EXP-ASYM-2 summarized in Table 1, are also performed to examine the sensitivity of TC intensification to differently prescribed asymptotic length scales. Figure 8 compares the simulated TC intensity and radial–height vortex structure from these three experiments. Interestingly, the sensitivity of TC intensification and structure to the asymptotic length scale is much weaker than that to the sloping curvature. This is somewhat a surprise considering that there are large differences in mixing lengths in the upper layers shown in Fig. 3c. The underlying reason will be explored in sections 5b and 5c.

To verify the robustness of the sensitivity of TC intensification and structural change to mixing length shown in the idealized TC simulations, we also performed HWRF real-case simulations of Hurricane Patricia (2015). The model configuration is exactly the same as that of the idealized simulations except that the initial and boundary conditions are supplied by the GFS forecast data. The simulations start at 0600 UTC 21 October and end at 1200 UTC 24 October 2015, when Patricia (215) dissipated after landfall. Again, five experiments summarized in Table 1 are executed to test the intensification and structural change of Patricia (2015) to the changes in the sloping curvature and asymptotic length scale of mixing length.

Figure 9 compares the simulated storm track, intensity, and vortex structure at different times among the three experiments with different sloping curvatures. The simulated storm

tracks of Patricia (2015) in the three experiments were fairly consistent with the best track throughout the simulations. The three experiments also produced nearly identical VMAX and MSLP before 2100 UTC 22 October consistent with the best track. After that, the simulated TC intensity diverged. EXP-SLOPE-1 nearly reproduced the observed RI and peak intensity of Patricia (2015), but BASELINE and EXP-SLOPE-2 underpredicted Patricia's intensity by a large margin. To understand what causes the simulated TC vortex to evolve along the different intensification pathways in the three experiments, we examined the structure of the simulated TC vortex. At 2100 UTC 22 October, the horizontal plane view of vertical velocity shows that the vortex in EXP-SLOPE-1 had a much more well-organized inner-core structure, including more axisymmetric eyewall and inner rainbands, than that in BASELINE and EXP-SLOPE-2 (Figs. 9e-g). The radialheight structures also show that EXP-SLOPE-1 produced the stronger azimuthal-mean tangential winds and radial inflow than BASELINE and EXP-SLOPE-2 (Figs. 9h-j), suggesting that the simulated vortex structure in EXP-SLOPE-1 was more favorable for the RI in the coming hours, despite the fact that this experiment produced the similar storm intensity to that of BASELINE and EXP-SLOPE-2 at 2100 UTC 22 October (Figs. 9b,c) after the model spinup. Satellite observations (e.g., Kieper and Jiang 2012; Jiang and Ramirez 2013; Tao and Jiang 2015) suggest that a convective ring around the storm center is highly correlated to the subsequent RI. A theoretical study by Nolan et al. (2007) also showed that TC intensification is mainly driven by the TC symmetric response to the azimuthally averaged diabatic heating, rather than to the heating directly associated with individual asymmetries distributed around the TC vortex. The simulation by EXP-SLOPE-1 basically reflects these observational and theoretical findings. In contrast, the simulated TC vortex in BASELINE and EXP-SLOPE-2 has a higher degree of asymmetry, which is adverse to RI. The simulated vortex horizontal and radius-height structures at 1100 UTC 23 October when Patricia was near its peak intensity are shown in Figs. 9k-p. The drastic difference in the vortex structure between the simulations suggests that differently parameterized turbulence via changes in the sloping curvature of mixing length can alter the TC intensification pathway under the same conditions.

Experiments have also been performed to examine the sensitivity of the simulated Patricia (2015) to the changes of the asymptotic length scale. The results are shown in Fig. 10. Similar to the idealized simulations (Fig. 8), the simulated Patricia (2015) is only marginally sensitive to the prescribed asymptotic length scale.

b. Mechanisms underlying TC intensification

In this section, we investigate the processes responsible for TC intensification. To do so, we analyzed the azimuth-mean tangential wind budget equation to diagnose how different dynamic processes contribute to the acceleration of primary circulation of a TC. The azimuth-mean tangential wind budget equation in a storm-centered cylindrical coordinate is

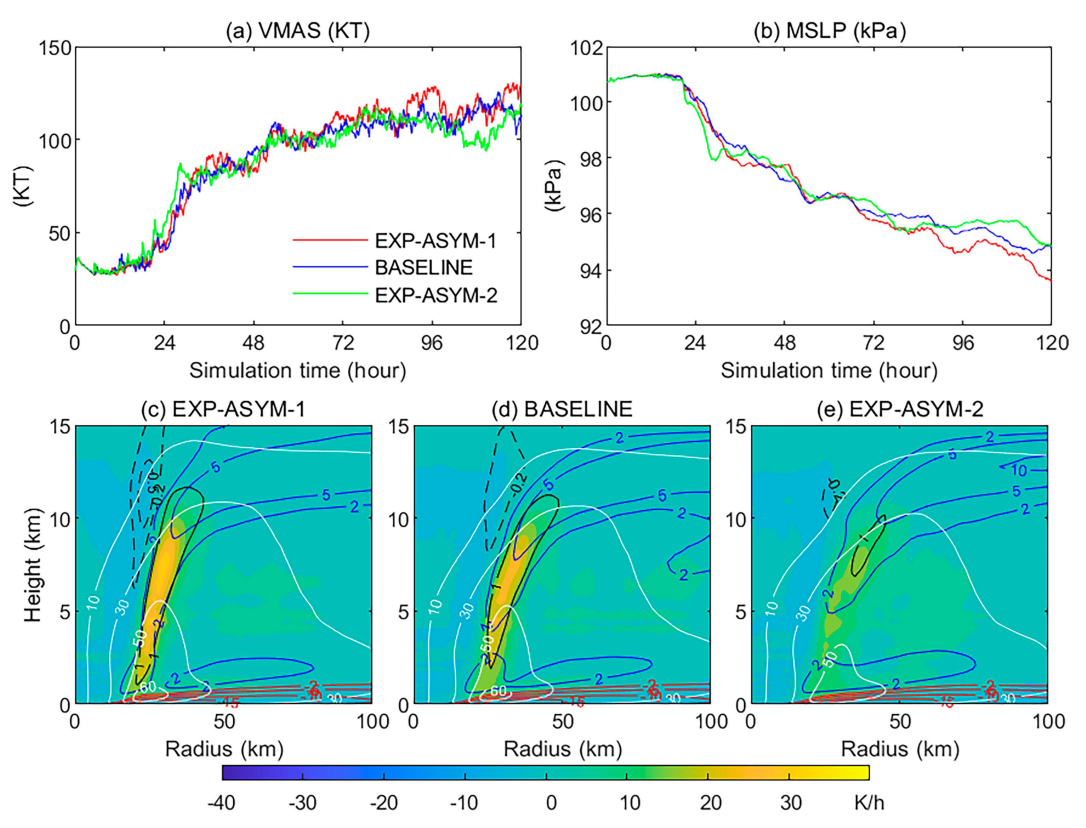


FIG. 8. Time series of (a) VMAX (KT) and (b) MSLP (kPa) from the three experiments: EXP-ASYM-1 (red), BASELINE (blue), and EXP-ASYM-2 (green), respectively. (c)–(e) Azimuthal-mean radius-height structure of diabatic heating (color shades; K h^{-1}); radial inflow (red contours; -2, -5, -10, -15, -20 m s $^{-1}$); radial outflow (blue contours; 2, 5, 10, 15, 20 m s $^{-1}$); updrafts (black contours; 1, 2, 5 m s $^{-1}$); downdrafts (black dashed contours; -0.2, -0.5 m s $^{-1}$); and tangential wind (white contours; 10, 30, 50, 60, 70, 80 m s $^{-1}$) averaged over the last 24 simulation hours.

$$\frac{\partial \overline{v_t}}{\partial t} = -\overline{u_r} \overline{\xi} - \overline{w} \frac{\partial \overline{v_t}}{\partial z} - \overline{u_r' \zeta'} - \overline{v_t'} \frac{\partial v_t'}{\partial \lambda} - \overline{w'} \frac{\partial v_t'}{\partial z} + D_{\text{sgs}\overline{\lambda}}. \quad (17)$$

Here, r, λ , and z are the axes in the radial, azimuthal, and vertical directions, respectively; u_r , v_t , and w are the radial, tangential, and vertical wind components respectively; overbar and prime indicate the azimuthal mean and the perturbations away from the azimuthal-mean; $\zeta = (\partial v_t/\partial r) + (v_t/r)$ and $\xi = \zeta$ + f are the relative vorticity and absolute vorticity, respectively; and f is the Coriolis parameter. The first two terms on the rhs of Eq. (17) are the tendencies resulting from the radial transport of the absolute vorticity and the vertical advection of tangential wind. These two terms represent the interaction between the primary circulation and secondary overturning circulation. The third, fourth, and fifth terms on the rhs of Eq. (17) are the tendencies from the eddy correlations caused by the model-resolved asymmetric eddies. The last term, $D_{sos\bar{\lambda}}$, represents the tendency resulting from the parameterized SGS turbulence and viscosity.

Using the model output, we analyzed the tangential wind budget of all the experiments performed in this study. As an example, Fig. 11 shows the budget analyses from EXP-SLOPE-1 averaged over the last 24 simulation hours. The

radial transport of absolute vorticity $-\overline{u_r}\xi$ generates large positive and negative tendencies within the inflow and outflow layers, respectively. This is because $\overline{\xi}$ is positive everywhere; thus, the sign of $-\overline{u_r}\xi$ is determined by the radial flow. The peak tendency occurs somewhere between the strongest inflow and maximum ξ depending on the specific structure of a vortex. Similarly, since \overline{w} is positive in the vicinity of RMW, the sign of $-\overline{w}(\partial \overline{v_t}/\partial z)$ is determined by the vertical gradient of tangential wind, which is positive and negative below and above the height of the peak tangential wind, respectively. Therefore, $-\overline{w}(\partial \overline{v_t}/\partial z)$ has a sign opposite to $-\overline{u_r}\xi$, causing the two terms to cancel each other. But analyses show that the magnitude of $-\overline{w}(\partial \overline{v_t}/\partial z)$ is overwhelmed by $-\overline{u_r}\xi$; thus, the net tendency induced by the mean secondary circulation $\left[-\overline{u_r}\overline{\xi} - \overline{w}(\partial \overline{v_r}/\partial z)\right]$ is to accelerate the primary circulation in the inflow layer near RMW.

The tendencies resulting from the eddy correlation of model-resolved asymmetric eddies $[-\overline{u_r'\zeta'} - \overline{v_l'(\partial v_l'/r\partial\lambda)} - \overline{w'(\partial v_l'/\partial z)}]$. Fig. 11c] is much smaller than the tendencies induced by the mean flow $[-\overline{u_r}\overline{\xi} - \overline{w}(\partial \overline{v_l}/\partial z)]$. This is consistent with Nolan et al. (2007) that TC intensification is mainly driven by the TC symmetric response to the azimuthally averaged diabatic heating. However, we note that the idealized simulations

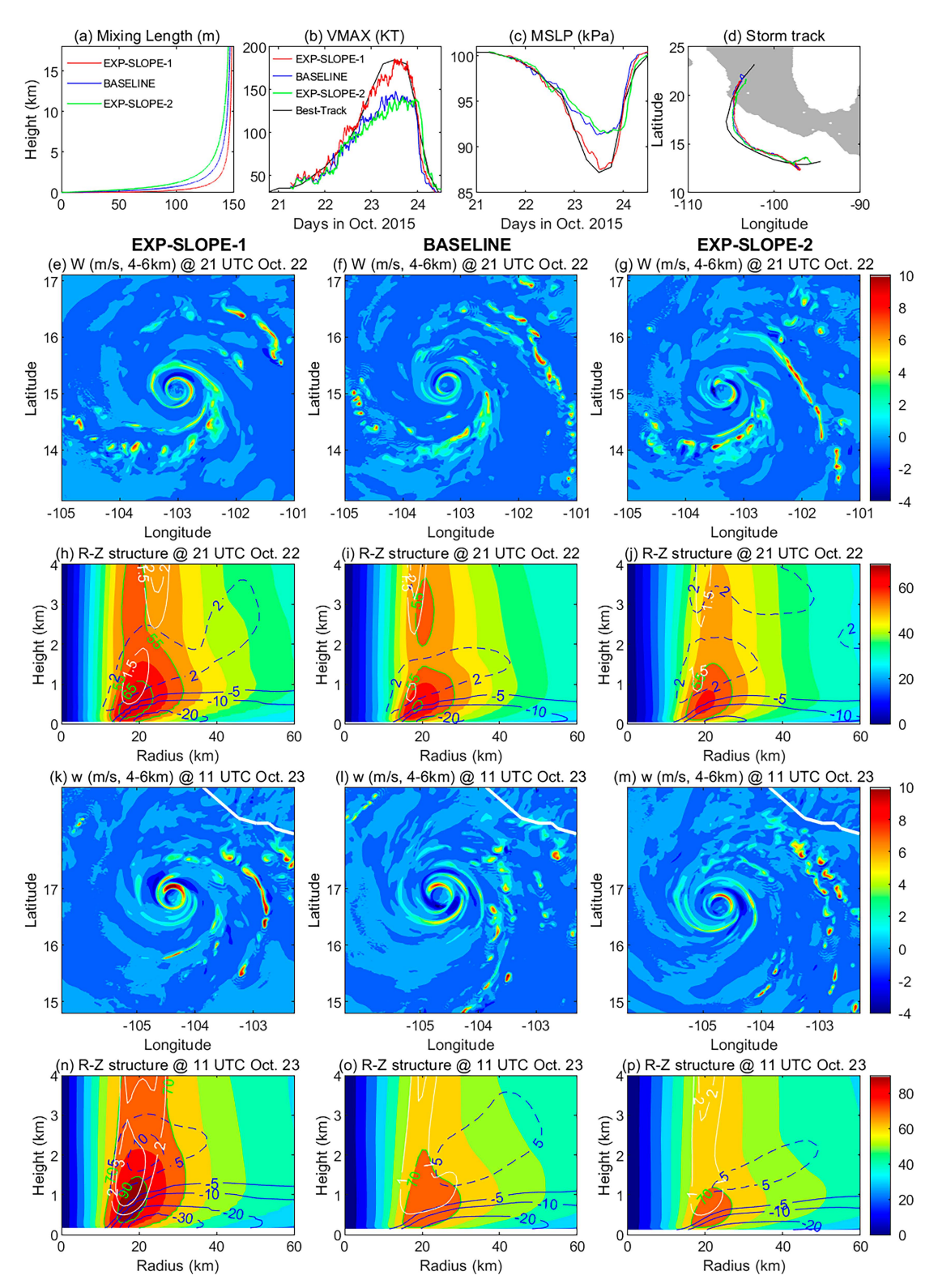


FIG. 9. (a) Vertical profiles of mixing lengths. (b) VMAX (KT). (c) MSLP (kPa). (d) Storm track. (e)–(g) Vertical velocity (m s⁻¹) averaged over the altitude of 4–6 km at 2100 UTC 22 Oct 2015, from EXP-SLOPE-1, BASELINE, and EXP-SLOPE-2, respectively. (h)–(j) The corresponding radial–height structure of azimuthal-mean tangential wind (m s⁻¹; green contours), radial flow (m s⁻¹; blue solid and dashed contours), and vertical velocity (m s⁻¹; white contours) at 2100 UTC 22 Oct. (k)–(m) As in (e)–(g), but at 1100 UTC 23 Oct. (n)–(p) As in (h)–(j), but at 1100 UTC 23 Oct.

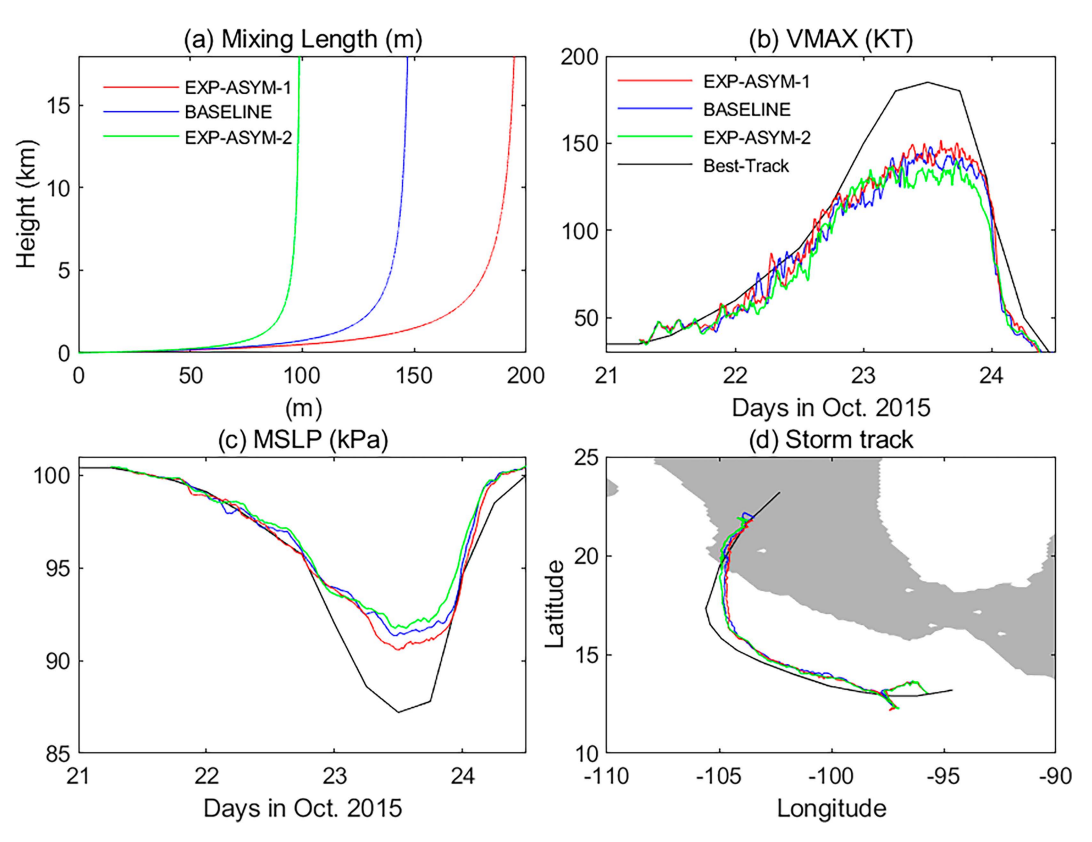


FIG. 10. (a) Vertical profiles of mixing lengths; (b) VMAX (KT); (c) MSLP (kPa); and (d) storm track of Hurricane Patricia (2015) simulated by EXP-ASYM-1, BASELINE, and EXP-ASYM-2, respectively.

were executed in a quiescent condition. The tendencies resulting from the resolved asymmetric eddies would be expected to be larger if wind shear was present. How wind shear affects the tangential wind budget will be investigated in our future study.

As shown in Fig. 11d, the tendency induced by $D_{\rm sgs\bar{\lambda}}$ is negative within the BL, which is the main momentum sink of a TC as expected. The radial-height structure of $D_{\rm sgs\bar{\lambda}}$ is consistent with that of Persing et al. (2013) and Zhu et al. (2019). The peak positive net tendency from all model-resolved and parameterized SGS processes corresponds well with the maximum tangential wind (Fig. 11e), which occurs just below the interface between the inflow and outflow near RMW consistent with the dropsonde observations (Zhang et al. 2020b).

The tangential wind budget analyses shown in Fig. 11 confirm that the inward transport of absolute vorticity is the main mechanism responsible for TC vortex acceleration consistent with the BL spinup mechanism by Smith et al. (2009). To understand how the same initial vortex evolves into different TCs in different experiments, Fig. 12 shows the radial–height structure of azimuthal-mean tangential wind, radial flow, vertical velocity, vertical moisture flux, net tendency of inward transport of absolute vorticity and eddy forcing $(-\overline{u_r}\xi + D_{\rm sgs}\overline{\lambda})$, and diabatic heating averaged over the time periods of 12–24, 25–36, 37–48, and 48–60 h from EXP-SLOPE-1, BASELINE, and EXP-SLOPE-2. In the period 12–24 h, the difference between the vortices in the three experiments is only marginal with similar

magnitude and structure of the tangential wind (gray contours) and radial inflow (red contours). At this stage, we only see a proto vortex without a clearly defined vortex eye and eyewall. Convection just clusters randomly around the center of the storm.

The proto vortex in different experiments starts to develop and undergoes different intensification pathways in the next 12 h (25-36 h). In EXP-SLOPE-1, a core of large tangential wind forms at a radius of ~20 km indicated by the closed contour of 14 m s⁻¹. The inflow layer thickens and reaches 1 km in altitude. The vortex in BASELINE is also somewhat strengthened (indicated by the tangential wind contour of $10 \,\mathrm{m \, s^{-1}}$ at ~ 30 –40 km in radius), but no core of large tangential wind is formed. The vortex in EXP-SLOPE-2 remains undeveloped. A key difference between the three experiments is the net tendency of $-\overline{u_r}\overline{\xi} + D_{\text{sgs}\overline{\lambda}}$. In EXP-SLOPE-1, $-\overline{u_r}\overline{\xi} + D_{\text{ses}\overline{\lambda}}$ (white contours) is positive, which accelerates the tangential wind. The increased tangential wind enhances surface evaporation and vertical moisture fluxes (blue contours), which fosters stronger convection indicated by the larger vertical velocity (black contours) and diabatic heating (color shades). The strong convection in turn further enhances radial inflow, and thus the inward transport of absolute vorticity. The fact that these processes go hand-in-hand suggests that a WISHE-like positive feedback has been kicked off, leading to the intensification of the vortex. In this feedback loop, it is

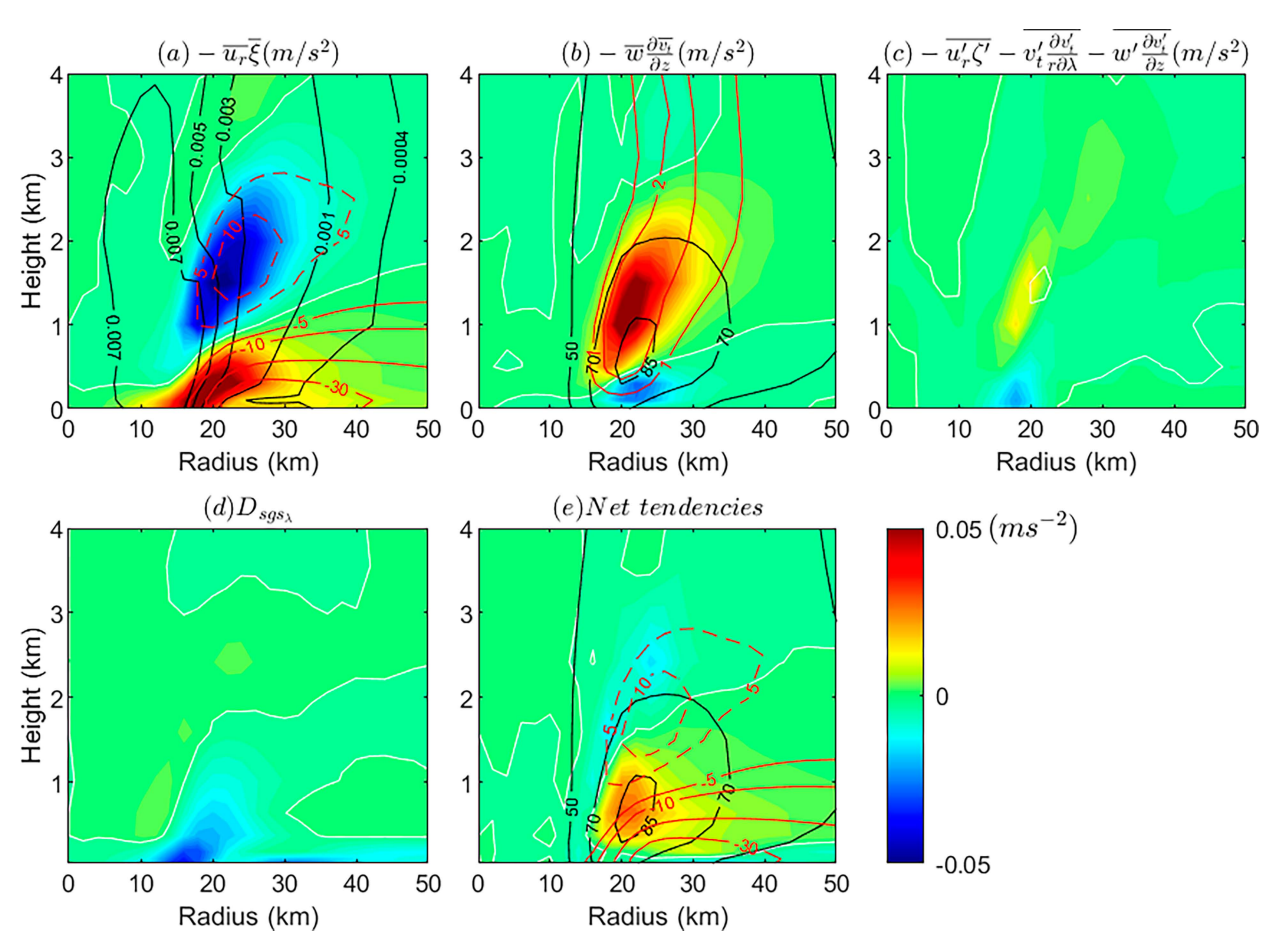


FIG. 11. Azimuthal-mean tangential wind tendencies (color shades, m s⁻²) induced by (a) $-\overline{u_r}\overline{\xi}$; (b) $-\overline{w}(\partial\overline{v_l}\partial z)$; (c) $-\overline{u_r'\zeta'} - \overline{v_l'(\partial v_l'/n\partial\lambda)} - \overline{w'(\partial v_l'/\partial z)}$; (d) $D_{sgs\overline{\lambda}}$; and (e) sum of (a)-(d) average over the last 24-h simulation of EXP-SLOPE-1. The black contours in (a) are $\overline{\xi}$ (0.4 × 10⁻³, 1 × 10⁻³, 3 × 10⁻³, 5 × 10⁻³, and 7 × 10⁻³ s⁻¹). Red solid and dashed contours in (a) and (e) are the radial flow $\overline{u_r}$ (-30, -20, -10, -5, 5, and 10 m s⁻¹). Red contours in (b) are the vertical velocity \overline{w} (1.0 and 2.0 m s⁻¹). Black contours in (b) and (e) are the tangential wind $\overline{v_r}$ (50, 70, and 85 m s⁻¹). White contours in all panels indicate the zero tendency.

difficult to distinguish the cause and outcome; rather, it is the interaction among different processes that initiates the feedback and governs the feedback efficiency.

In the next 12 h (37–48 h), the vortex in EXP-SLOPE-1 keeps strengthening owing to the WISHE-like positive feedback. The tangential wind increases up to 35 m s⁻¹. As the vortex further organizes itself, the convection at the storm center in the previous time period (25-36 h) dissipates and moves outward. This forms a vortex eye free of convection and convective eyewall. Similar development is also seen in BASELINE, but the vortex is weaker than that of EXP-SLOPE-1. Apparently, the WISHE-like positive feedback is not as efficient as that in EXP-SLOPE-1. Still, there is no visible vortex development in EXP-SLOPE-2 at this stage. In the next 12 h (49–60 h), the vortex in EXP-SLOPE-1 continues intensifying. The maximum tangential wind exceeds 50 m s⁻¹, and the eyewall becomes more organized as the convection becomes more intense. The vortex in BASELINE also strengthens but is weaker than that in EXP-SLOPE-1. The vortex in EXP-SLOPE-2 also starts to develop in this period,

but its strength is nowhere close to that of EXP-SLOPE-1 and BASELINE.

A key difference between experiments shown in Fig. 12 is the net tendency of $-\overline{u_r}\overline{\xi} + D_{sgs\overline{\lambda}}$, which is important to the feedback loop since it directly affects the acceleration of the mean vortex. Therefore, we further examined how this tendency evolves throughout the entire simulations. A time evolution plot is provided in the online supplemental material (Fig. S2). The results show that $-\overline{u_r}\overline{\xi}$ maintains its dominance over $D_{sos\overline{\lambda}}$ throughout the simulation in EXP-SLOPE-1. In contrast, $-\overline{u_r}\xi$ is nearly balanced by $D_{sgs\overline{\lambda}}$ in BASELINE, whereas in EXP-SLOPE-2, $-\overline{u_r}\xi$ is unable to compensate for the negative $D_{{\rm sgs}\overline{\lambda}}.$ This result suggests that the secondary overturning circulation induced by the turbulent friction and eyewall convection must exceed a critical level, so that sufficiently large inward transport of absolute vorticity can be generated to overcome the negative tendencies so that the WISHE-like positive feedback can be kicked off. To investigate what determines this critical level and how to quantify it from model output will be the focus of our future research.

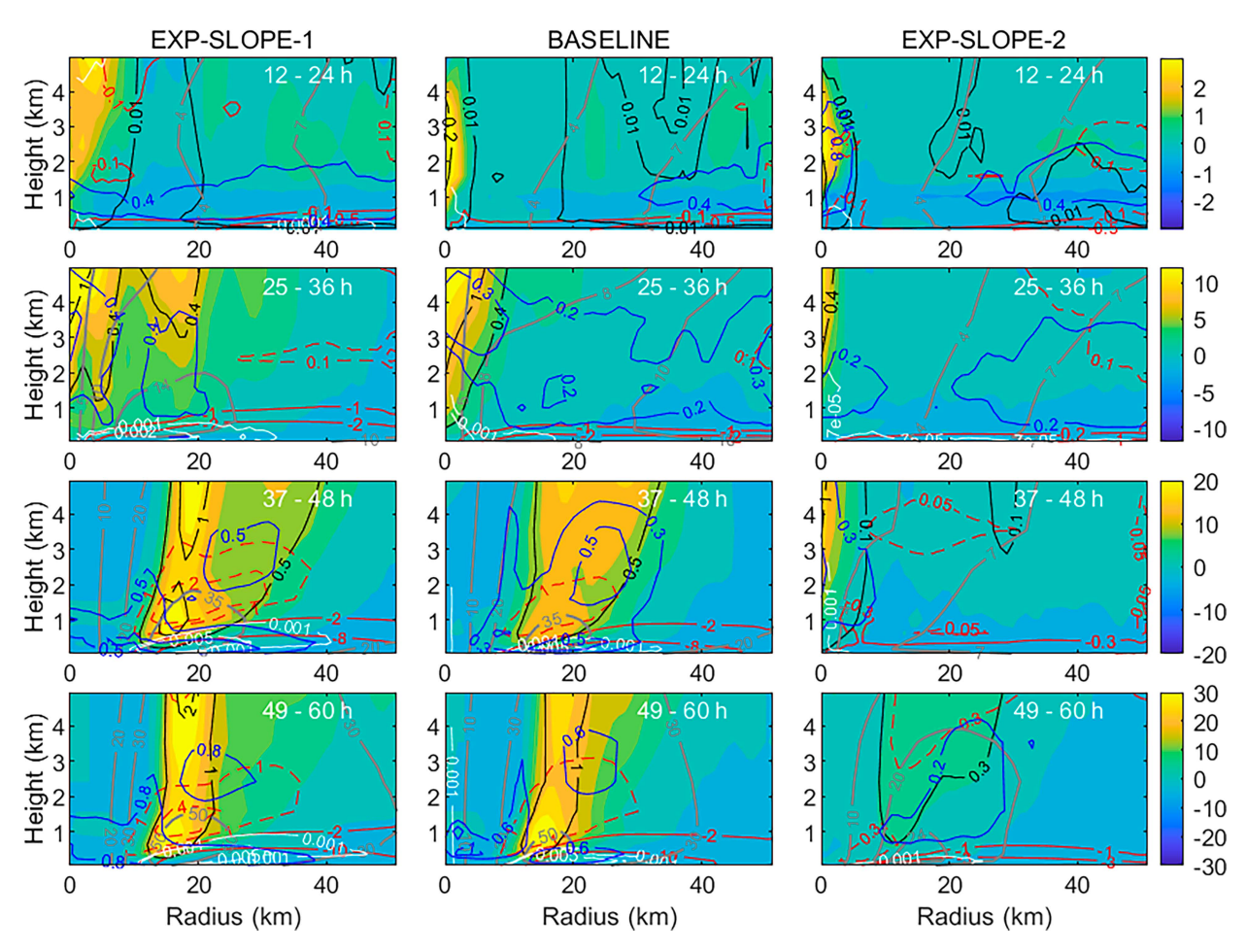


FIG. 12. Radial-height structure of azimuthal-mean tangential wind (gray contours), radial flow (red solid and dashed contours), vertical velocity (black contours), vertical moisture flux (blue contours), the sum of tendencies induced by the mean radial transport of absolute vorticity and tangential eddy forcing $(-\overline{u_r}\overline{\xi} + D_{sgs\bar{\lambda}})$, white contours), and diabatic heating (color shades) averaged over the time periods of 12–24, 25–36, 37–48, and 48–60 h from experiments EXP-SLOPE-1, BASELINE, and EXP-SLOPE-2.

The same budget analyses have also been performed for the HWRF real-case simulations of Patricia (2015), and similar results are found, confirming that the WISHE-like positive feedback is a key mechanism underlying TC intensification.

c. Reasons for sensitive dependence of TC intensification on mixing length in TKE schemes

The sensitivity of TC intensification to mixing length shown in section 5a is interesting but not well understood. The TKE scheme presented in section 2 allows us to explore this issue analytically. To simplify the problem, we first set an idealized vertical profile of wind speed in a TC environment based on the observations and simulations (Fig. 13a) and then select two Richardson numbers, $R_i = -0.5$ and $R_i = 0.1$, to represent the unstable and stable regimes in the TC inner core. For a known R_i , the dimensionless stability parameter G_h and stability functions S_m and S_h can be calculated from Eqs. (7) and (2), respectively. Table 2 lists all the calculated parameters.

For certain prescribed mixing lengths, the TKE generated under a specific wind profile (Fig. 13a) and thermodynamic conditions (Table 2) can be calculated from Eq. (6). Figures 13c and 13d show the resultant TKE profiles corresponding to the mixing lengths used in EXP-SLOPE-1, BASELINE, and EXP-SLOPE-2, respectively. As indicated in Eq. (6), under certain dynamic and thermodynamic conditions, TKE is proportional to the square of mixing length and square of wind shear. Since both wind shear and changes in the mixing length caused by the sloping curvature are the largest in the low troposphere, they amplify each other. The combination causes the strong sensitivity of TKE to the sloping curvature of mixing length.

The sensitivity of TKE to mixing lengths with similar sloping curvatures but different asymptotic length scales is also examined under the same dynamic and thermodynamic conditions (Fig. 14). Unlike what is shown in Fig. 13, the parameterized TKE only shows a marginal sensitivity to the asymptotic length. Again, this insensitivity is determined by the combination of both wind shear and mixing length

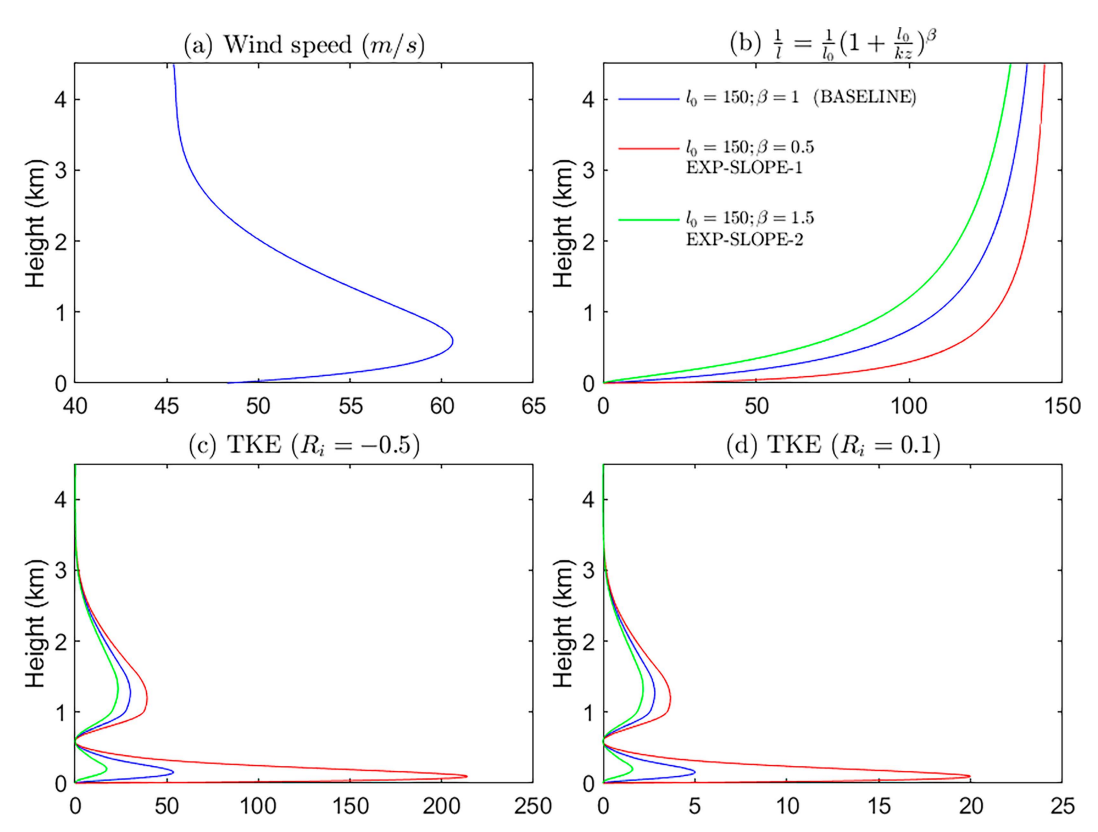


FIG. 13. (a) Idealized vertical profile of wind speed in the eyewall. (b) Mixing lengths used in the three experiments: EXP-SLOPE-1, BASELINE, and EXP-SLOPE-2. (c),(d) TKE generated for the idealized vertical profile of wind speed and Richardson numbers of $R_i = -0.5$ and 0.1 for different mixing lengths.

structure. Large wind shear is in the BL, but the difference in the mixing length corresponding to the large wind shear is small due to the similar sloping curvature in the BL, leading to the insensitiveness of TKE to mixing length. On the other hand, above the BL, differences in the mixing length are large due to the differently prescribed asymptotic length scales, but the wind shear is small there. The combination again results in the weak dependence of TKE on the asymptotic length scale.

Note that the idealized TKE profiles in Figs. 13 and 14 cannot be directly compared to those in Fig. 7. This is because the former is calculated with the prescribed $R_i = N^2/S^2 = -0.5$, 0.1, so that TKE is solely determined by the wind shear and mixing length. In Fig. 7, however, TKE is calculated using the simulated soundings averaged over the eyewall (taken as the area of r > 0.7 RMW). Therefore, TKE profiles are not only determined by l^2 and S^2 but also depend largely on how N^2 , S_m , and S_h vary with height and radius. A detailed description of how to

TABLE 2. Parameters used to examine the sensitivity of TKE to turbulent mixing length.

R_i	G_h	S_m	S_h
-0.5	0.0180	1.0123	1.3173
0.1	-0.0386	0.1772	0.2112

obtain TKE profiles in Fig. 7 is provided in the supplemental material.

In a TKE scheme, eddy diffusivity $(K_m \text{ and } K_h)$ is proportional to TKE according to Eq. (3). Indeed, EXP-SLOPE-1 does produce larger K_m and K_h corresponding to the larger TKE than the other experiments (not shown here). This result seems contradictory to previous studies showing that smaller K_m favors TC intensification (e.g., Gopalakrishnan et al. 2013; Zhang et al. 2020a; Xu and Duan 2022). There are a couple of reasons for this seeming contradiction. First, the relationship between K_m and TC intensification is likely scheme dependent. In Gopalakrishnan et al. (2013) and Zhang et al. (2020a), their simulations used a K-closure model that calculates K_m in a completely different way. In MY level-2 model, K_m is analytically linked to TKE, mixing length, wind shear, and stability, which allows us to examine how they affect each other in TC simulations. Considering that for the same MY TKE scheme, a slight change in the mixing length curvature can cause substantially different TC intensification, it is not a surprise that TC intensification could respond oppositely to a differently formulated K_m . This can be seen from the direct impact of K_m on the acceleration of a TC vortex via the tendency resulting from turbulence. Using $\partial \overline{u}/\partial t = \cdots +$ $(\partial/\partial z)[K_m(\partial \overline{u}/\partial z)]$ as an example, the tendency induced by turbulence may be split into two terms:

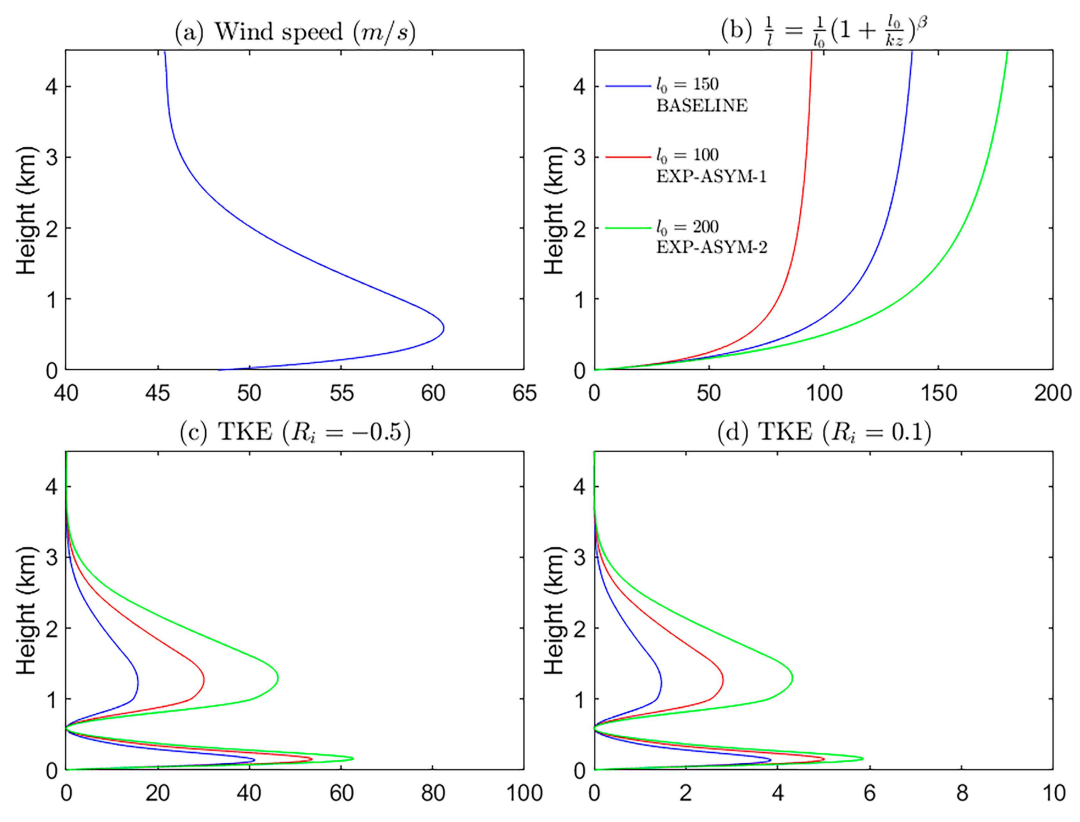


FIG. 14. As in Fig. 13, but for the experiments EXP-ASYM-1, BASELINE, and EXP-ASYM-2.

$$\frac{\partial}{\partial z} \left(K_m \frac{\partial \overline{u}}{\partial z} \right) = K_m \frac{\partial^2 \overline{u}}{\partial z^2} + \frac{\partial K_m}{\partial z} \frac{\partial \overline{u}}{\partial z}. \tag{18}$$

further looking into Eq. (18). With Eqs. (3) and (6), Eq. (18) becomes

It suggests that both the magnitude and vertical gradient of K_m can directly affect velocity tendencies. For simplicity, let us consider the surface layer. If the winds follow the log profile, then $\partial^2 \overline{u}/\partial z^2 < 0$. Since both $\partial \overline{u}/\partial z$ and $\partial K_m/\partial z$ are positive, terms $K_m(\partial^2 \overline{u}/\partial z^2)$ and $(\partial K_m/\partial z)(\partial \overline{u}/\partial z)$ have the opposite signs and they tend to cancel each other. If the first term $K_m(\partial^2 \overline{u}/\partial z^2)$ would dominate, then, smaller K_m could favor TC intensification since the negative $K_m(\partial^2 \overline{u}/\partial z^2)$ would exert a smaller frictional force on the turbulent flow. On the other hand, larger K_m could also favor TC intensification via term $(\partial K_m/\partial z)(\partial \overline{u}/\partial z)$ as it tends to counteract the negative $K_m(\partial^2 \overline{u}/\partial z^2)$. The net effect depends on how K_m is parameterized that determines its magnitude and vertical gradient.

Second, it is not a single process but the feedback among many processes that ultimately governs the route to TC intensification. As discussed earlier, K_m can also affect TC intensification indirectly through the inward transport of absolute vorticity by the inflow. To date, it remains poorly understood as to how K_m modulates the feedback underlying the TC intensification. Therefore, the seeming contradictory results between this study and previous studies state nothing but the complicated relationship between TC simulation and turbulence parameterization.

As for why TC simulations are so sensitive to the sloping curvature of mixing length, we may get some new insight by

$$\begin{split} \frac{\partial}{\partial z} \left(K_m \frac{\partial \overline{u}}{\partial z} \right) &= l^2 \frac{\partial}{\partial z} \left[S S_m \sqrt{b_1 (S_m - S_h R_i)} \frac{\partial \overline{u}}{\partial z} \right] \\ &+ 2 l S S_m \sqrt{b_1 (S_m - S_h R_i)} \frac{\partial l}{\partial z} \frac{\partial \overline{u}}{\partial z} \,. \end{split} \tag{19}$$

It is clear that the tendency depends on both the magnitude and slope of the mixing length l. In the lower layers where l is small and velocity curvature $\partial^2 \overline{u}/\partial z^2$ is smaller than gradient $\partial \overline{u}/\partial z$, the tendency induced by turbulence will be largely affected by the slope $\partial l/\partial z$ and further modulated by wind shear and stability. This may explain why the larger/smaller sloping curvature of l can produce the stronger/weaker TC vortex in EXP-SLOPE-1 and EXP-SLOPE-2, respectively. Furthermore, considering that there is also an indirect impact of mixing length on wind tendencies via the radial transport of absolute vorticity, the problem becomes too complicated to assess analytically. Thus, we have to rely on numerical sensitivity tests to determine the net effect of mixing length on TC intensification. Our sensitivity tests suggest that a large sloping curvature of mixing length favors TC intensification as it enhances the inward transport of absolute vorticity, which plays a pivotal role in kicking off the WISHE-like positive feedback underlying TC intensification and increasing the feedback efficiency.

6. Summary and discussion

It has long been recognized that the turbulent eddy processes play a vital role in the evolution of the primary and secondary circulations of a TC vortex. In a TC environment, in addition to the turbulence in the BL, intense turbulent mixing can also be generated above the BL by the cloud processes in the eyewall and rainbands. While the concept of BL is still applicable in the eyewall and rainbands as to a shallow layer directly affected by the surface processes, the treatment of turbulent mixing must go beyond the conventional scope of the BL. This is particularly true in the TC inner core as air ascends swiftly within the eyewall and rainbands. Indeed, observations confirm that large TKEs extend well above the BL and reach the upper troposphere in the eyewall where no physical interface exists to separate the turbulence generated by the BL and cloud processes aloft. A TKE turbulence scheme is suitable for parameterizing turbulence in the TC inner core as it is applicable to both deep and shallow convection regimes provided that the TKE shear production, buoyancy production, and dissipation can be accurately determined. However, a TKE scheme must be closed by an empirically prescribed mixing length. To date, how the prescribed mixing length affects TC simulation remains poorly understood. This motivates this study to investigate the sensitivity of TC intensification to differently prescribed mixing length.

To appropriately address the problem, we transformed the MY level-2 model (MY1974; MY1982) into a moist TKE scheme that considers the saturated thermodynamics by including the buoyancy generated by mixed-phase clouds in the stability calculation, so that the scheme can be appropriately applied to the TC inner core. The reason for choosing the MY level-2 model is that this simplification allows us to analytically diagnose TKE as a function of wind shear, static stability, and mixing length. This provides a mathematical way to understand the sensitivity of simulated TC intensification to the mixing length.

Both idealized and real-case TC simulations show that TC intensification is sensitive to the sloping curvature of mixing length in the low- to midtroposphere where the larger increase of mixing length leads to the faster intensification and stronger storm intensity. This is due to the fact that TKE is proportional to the square of mixing length and wind shear. The combined effect of large changes in mixing length and wind shear in the low- to midtroposphere causes the strong sensitivity of the simulated TKE to the sloping curvature of mixing length. Since the radial inflow depends strongly on the generated TKE in the vicinity of the eyewall, the resultant large change in the inward transport of absolute vorticity, a main mechanism for the acceleration of TC primary circulation, causes the TC intensification to be sensitive to the sloping curvature of mixing length. On the other hand, since the difference in the mixing length in the upper troposphere caused by different asymptotic length scales is largely offset by the small wind shear there, it results in a weak dependence of TKE and the resultant inward transport of absolute vorticity on the asymptotic length scale.

Note that for the sake of simplification of the problem, we chose a diagnostic TKE scheme developed from the MY

level-2 model. Thus, the sensitivity of TC intensification to mixing length from a sophisticated prognostic TKE scheme may be different from the sensitivity shown in this study based on a simple model. Nonetheless, the results shown here emphasize the uncertainty and importance of mixing length in TC simulations. It is also important to point out that most formulae of mixing length, including Eqs. (12)-(14) tested in this study, were originally formulated for cloud-free BL simulations. Mixing length inside deep convective clouds has been explored very little. Machado and Chaboureau (2015) showed that the simulations of cloud organizations are highly sensitive to in-cloud mixing length parameterization and adjustments of mixing length inside clouds can substantially affect the simulation of cloud organizations. Hanley et al. (2015) also investigated the sensitivity of storm morphology to mixing length. These studies suggest that future research should focus on searching for physical constraints including the effect of convective clouds on mixing length using observations and LESs.

Finally, this study highlights the importance of the inward transport of absolute vorticity resulting from the unbalanced dynamics to TC intensification. However, how the parameterized turbulent processes affect the unbalanced dynamics in TC intensification is not fully understood. The related issues are addressed in part II of this study.

Acknowledgments. This work is supported by NOAA/JTTI program under Grant NA22OAR4590177 and National Science Foundation under Grant 2211307. We are very grateful to the three anonymous reviewers for their constructive and insightful comments, which led to the improvement of the paper.

Data availability statement. The simulation data generated by this study can be accessed at http://vortex.ihrc.fiu.edu/download/TC_turbulent_processes/.

REFERENCES

Aligo, E. A., B. Ferrier, and J. R. Carley, 2018: Modified NAM microphysics for forecasts of deep convective storms. *Mon. Wea. Rev.*, 146, 4115–4153, https://doi.org/10.1175/MWR-D-17-0277.1.

Charney, J. G., and A. Eliassen, 1964: On the growth of the hurricane depression. *J. Atmos. Sci.*, **21**, 68–75, https://doi.org/10. 1175/1520-0469(1964)021<0068:OTGOTH>2.0.CO;2.

Chen, X., and G. H. Bryan, 2021: Role of advection of parameterized turbulence kinetic energy in idealized tropical cyclone simulations. *J. Atmos. Sci.*, 78, 3593–3611, https://doi.org/10. 1175/JAS-D-21-0088.1.

—, —, J. A. Zhang, J. J. Cione, and F. D. Marks, 2021: A framework for simulating the tropical cyclone boundary layer using large-eddy simulation and its use in evaluating PBL parameterizations. *J. Atmos. Sci.*, 78, 3559–3574, https://doi.org/10.1175/JAS-D-20-0227.1.

Dunion, J. P., and C. S. Marron, 2008: A reexamination of the Jordan mean tropical sounding based on awareness of the Saharan air layer: Results from 2002. J. Climate, 21, 5242–5253, https://doi.org/10.1175/2008JCL11868.1.

- Emanuel, K. A., 1986: An air-sea interaction theory for tropical cyclones. Part I: Steady-state maintenance. *J. Atmos. Sci.*, **43**, 585–605, https://doi.org/10.1175/1520-0469(1986)043<0585: AASITF>2.0.CO:2.
- Galperin, B., L. H. Kantha, S. Hassid, and A. Rosati, 1988: A quasi-equilibrium turbulent energy model for geophysical flows. *J. Atmos. Sci.*, **45**, 55–62, https://doi.org/10.1175/1520-0469(1988)045<0055:AQETEM>2.0.CO;2.
- Gopalakrishnan, S. G., F. Marks Jr., J. A. Zhang, X. Zhang, J.-W. Bao, and V. Tallapragada, 2013: A study of the impacts of vertical diffusion on the structure and intensity of the tropical cyclones using the high-resolution HWRF system. *J. Atmos. Sci.*, 70, 524–541, https://doi.org/10.1175/JAS-D-11-0340.1.
- Gopalakrishnan, S., A. Hazelton, and J. A. Zhang, 2021: Improving hurricane boundary layer parameterization scheme based on observations. *Earth Space Sci.*, 8, e2020EA001422, https://doi.org/10.1029/2020EA001422.
- Grenier, H., and C. S. Bretherton, 2001: A moist PBL parameterization for large-scale models and its application to subtropical cloud-topped marine boundary layers. *Mon. Wea. Rev.*, **129**, 357–377, https://doi.org/10.1175/1520-0493(2001)129 <0357:AMPPFL>2.0.CO;2.
- Han, J., and C. S. Bretherton, 2019: TKE-based moist eddydiffusivity mass-flux (EDMF) parameterization for vertical turbulent mixing. Wea. Forecasting, 34, 869–886, https:// doi.org/10.1175/WAF-D-18-0146.1.
- —, M. L. Witek, J. Teixeira, R. Sun, H.-L. Pan, J. K. Fletcher, and C. S. Bretherton, 2016: Implementation in the NCEP GFS of a hybrid eddy-diffusivity mass-flux (EDMF) boundary layer parameterization with dissipative heating and modified stable boundary layer mixing. Wea. Forecasting, 31, 341–352, https://doi.org/10.1175/WAF-D-15-0053.1.
- Hanley, K. E., R. S. Plant, T. H. M. Stein, R. J. Hogan, J. C. Nicol, H. W. Lean, C. Halliwell, and P. A. Clark, 2015: Mixing-length controls on high-resolution simulations of convective storms. *Quart. J. Roy. Meteor. Soc.*, 141, 272–284, https://doi.org/10.1002/qj.2356.
- Hazelton, A., J. A. Zhang, and S. Gopalakrishnan, 2022: Comparison of the performance of the observation-based hybrid EDMF and EDMF-TKE PBL schemes in 2020 tropical cyclone forecasts from the global-nested Hurricane Analysis and Forecast System. Wea. Forecasting, 37, 457–476, https://doi.org/10.1175/WAF-D-21-0124.1.
- Hong, S.-Y., and H.-L. Pan, 1996: Nonlocal boundary layer vertical diffusion in a medium-range forecast model. *Mon. Wea. Rev.*, **124**, 2322–2339, https://doi.org/10.1175/1520-0493(1996) 124<2322:NBLVDI>2.0.CO;2.
- —, Y. Noh, and J. Dudhia, 2006: A new vertical diffusion package with an explicit treatment of entrainment processes. Mon. Wea. Rev., 134, 2318–2341, https://doi.org/10.1175/MWR3199.1
- Jiang, H., and E. M. Ramirez, 2013: Necessary conditions for tropical cyclone rapid intensification as derived from 11 years of TRMM data. *J. Climate*, 26, 6459–6470, https://doi.org/10.1175/JCLI-D-12-00432.1.
- Jordan, C. L., 1958: Mean soundings for the West Indies area. J. Atmos. Sci., 15, 91–97, https://doi.org/10.1175/1520-0469(1958) 015<0091:MSFTWI>2.0.CO;2.
- Katz, J., and P. Zhu, 2024: Parameterization of vertical turbulent transport in the inner core of tropical cyclones and its impact on storm intensification. Part II: Understanding TC intensification in a generalized Sawyer–Eliassen diagnostic framework.

- *J. Atmos. Sci.*, **81**, 1769–1782, https://doi.org/10.1175/JAS-D-23-0243.1.
- Kieper, M. E., and H. Jiang, 2012: Predicting tropical cyclone rapid intensification using the 37 GHz ring pattern identified from passive microwave measurements. *Geophys. Res. Lett.*, 39, L13804, https://doi.org/10.1029/2012GL052115.
- Li, Y., P. Zhu, Z. Gao, K. K. W. Cheung, 2022: Sensitivity of large eddy simulations of tropical cyclone to sub-grid scale mixing parameterization. *Atmos. Res.*, 265, 105922, https://doi.org/10. 1016/j.atmosres.2021.105922.
- Lorsolo, S., J. A. Zhang, F. Marks Jr., and J. Gamache, 2010: Estimation and mapping of hurricane turbulent energy using airborne Doppler measurements. *Mon. Wea. Rev.*, 138, 3656–3670, https://doi.org/10.1175/2010MWR3183.1.
- Machado, L. A. T., and J.-P. Chaboureau, 2015: Effect of turbulence parameterization on assessment of cloud organization. *Mon. Wea. Rev.*, 143, 3246–3262, https://doi.org/10.1175/ MWR-D-14-00393.1.
- Marks, F. D., P. G. Black, M. T. Montgomery, and R. W. Burpee, 2008: Structure of the eye and eyewall of Hurricane Hugo (1989). Mon. Wea. Rev., 136, 1237–1259, https://doi.org/10. 1175/2007MWR2073.1.
- Mellor, G. L., and T. Yamada, 1974: A hierarchy of turbulence closure models for planetary boundary layers. *J. Atmos. Sci.*, 31, 1791–1806, https://doi.org/10.1175/1520-0469(1974)031 <1791:AHOTCM>2.0.CO;2.
- —, and —, 1982: Development of a turbulence closure model for geophysical fluid problems. *Rev. Geophys.*, **20**, 851–875, https://doi.org/10.1029/RG020i004p00851.
- Montgomery, M. T., and R. K. Smith, 2014: Paradigms for tropical cyclone intensification. *Aust. Meteor. Ocean J.*, 64, 37–66, https://doi.org/10.22499/2.6401.005.
- Moss, M. S., and S. L. Rosenthal, 1975: On the estimation of planetary boundary layer variables in mature hurricanes. *Mon. Wea. Rev.*, **103**, 980–988, https://doi.org/10.1175/1520-0493 (1975)103<0980:OTEOPB>2.0.CO:2.
- Nakanish, M., 2001: Improvement of the Mellor-Yamada turbulence closure model based on large-eddy simulation data. Bound.-Layer Meteor., 99, 349–378, https://doi.org/10.1023/A: 1018915827400.
- Nolan, D. S., and M. T. Montgomery, 2002: Nonhydrostatic, three-dimensional perturbations to balanced, hurricane-like vortices. Part I: Linearized formulation, stability, and evolution. J. Atmos. Sci., 59, 2989–3020, https://doi.org/10.1175/ 1520-0469(2002)059<2989:NTDPTB>2.0.CO;2.
- —, Y. Moon, and D. P. Stern, 2007: Tropical cyclone intensification from asymmetric convection: Energetics and efficiency. *J. Atmos. Sci.*, 64, 3377–3405, https://doi.org/10.1175/JAS3988.1.
- Ooyama, K. V., 1964: A dynamical model for the study of tropical cyclone development. *Geofis. Int.*, 4, 187–198, https://doi.org/ 10.22201/igeof.2954436xe.1964.4.4.1671.
- —, 1982: Conceptual evolution of the theory and modeling of the tropical cyclone. *J. Meteor. Soc. Japan*, **60**, 369–380, https://doi.org/10.2151/jmsj1965.60.1_369.
- Persing, J., M. T. Montgomery, J. C. McWilliams, and R. K. Smith, 2013: Asymmetric and axisymmetric dynamics of tropical cyclones. *Atmos. Chem. Phys.*, 13, 12299–12341, https://doi.org/10.5194/acp-13-12299-2013.
- Pleim, J. E., 2007: A combined local and nonlocal closure model for the atmospheric boundary layer. Part II: Application and evaluation in a mesoscale meteorological model. *J. Appl. Meteor. Climatol.*, 46, 1396–1409, https://doi.org/10.1175/ JAM2534.1.

- Pope, S. B., 2000: *Turbulent Flows*. 1st ed. Cambridge University Press, 802 pp., https://doi.org/10.1017/CBO9780511840531.
- Shapiro, L. J., 1983: The asymmetric boundary layer flow under a translating hurricane. *J. Atmos. Sci.*, **40**, 1984–1998, https://doi.org/10.1175/1520-0469(1983)040<1984:TABLFU>2.0.CO;2.
- Smith, R. K., and M. T. Montgomery, 2010: Hurricane boundary-layer theory. *Quart. J. Roy. Meteor. Soc.*, **136**, 1665–1670, https://doi.org/10.1002/qj.679.
- —, and S. Vogl, 2008: A critique of Emanuel's hurricane model and potential intensity theory. *Quart. J. Roy. Meteor. Soc.*, **134**, 551–561, https://doi.org/10.1002/qj.241.
- ——, and N. Van Sang, 2009: Tropical cyclone spin-up revisited. *Quart. J. Roy. Meteor. Soc.*, **135**, 1321–1335, https://doi.org/10.1002/qj.428.
- Stull, R. B., 1988: An Introduction to Boundary Layer Meteorology. Kluwer, 666 pp.
- Tao, C., and H. Jiang, 2015: Distributions of shallow to very deep precipitation–convection in rapidly intensifying tropical cyclones. J. Climate, 28, 8791–8824, https://doi.org/10.1175/JCLI-D-14-00448.1.
- Wood, V. T., and L. W. White, 2011: A new parametric model of vortex tangential-wind profiles: Development, testing, and verification. *J. Atmos. Sci.*, 68, 990–1006, https://doi.org/10. 1175/2011JAS3588.1.
- Xu, H., and Y. Duan, 2022: Sensitivity of the tropical cyclone boundary layer to vertical diffusion in a turbulent kinetic energy-based boundary layer parameterization scheme at gray-zone

- resolution. J. Geophys. Res. Atmos., **127**, e2021JD035601, https://doi.org/10.1029/2021JD035601.
- Zhang, J. A., E. A. Kalina, M. K. Biswas, R. F. Rogers, P. Zhu, and F. D. Marks, 2020a: A review and evaluation of planetary boundary layer parameterizations in Hurricane Weather Research and Forecasting model using idealized simulations and observations. *Atmosphere*, 11, 1091, https://doi.org/10.3390/atmos11101091.
- —, J. P. Dunion, and D. S. Nolan, 2020b: In-situ observations of the diurnal variation in the boundary layer of mature hurricanes. *Geophys. Res. Lett.*, 47, 2019GL086206, https://doi.org/10.1029/2019GL086206.
- Zhu, P., and Coauthors, 2015: Impact of subgrid-scale processes on eyewall replacement cycle of tropical cyclones in HWRF system. *Geophys. Res. Lett.*, 42, 10 027–10 036, https://doi.org/ 10.1002/2015GL066436.
- ——, B. Tyner, J. A. Zhang, E. Aligo, S. Gopalakrishnan, F. D. Marks, A. Mehra, and V. Tallapragada, 2019: Role of eyewall and rainband eddy forcing in tropical cyclone intensification. *Atmos. Chem. Phys.*, 19, 14289–14310, https://doi.org/10.5194/acp-19-14289-2019.
- —, A. Hazelton, Z. Zhang, F. D. Marks, and V. Tallapragada, 2021: The role of eyewall turbulent transport in the pathway to intensification of tropical cyclones. *J. Geophys. Res. Atmos.*, 126, e2021JD034983, https://doi.org/10.1029/2021JD034983.